https://doi.org/10.5194/egusphere-2025-4773
Preprint. Discussion started: 19 December 2025

Wave effect mechanisms enhancing sea–air CO_2 exchange and modulating seawater carbonate–pH adaptation in the POP2–waves coupled model

Yung-Yao Lan, Huang-Hsiung Hsu, Wei-Liang Lee* and Simon Chou
Research Center for Environmental Changes, Academia Sinica, Taipei 11529, Taiwan
Correspondence to: Wei-Liang Lee (leelupin@gate.sinica.edu.tw)

Abstract

Wave and bubble mechanisms have demonstrated their impact on sea–air CO_2 flux by enhancing gas transfer velocity (K_w) through significant wave height (H_s). Neglecting wave and bubble processes may lead to an underestimation of CO_2 flux under high 10-m wind speeds (U_{10}) in most state-of-the-art climate models. In this study, a waves module from the Princeton Ocean Model (POM) has been incorporated into the Parallel Ocean Program version 2 (POP2), referred to as POP2–waves, in the Community Earth System Model version 1.2.2 (CESM1.2.2) framework. The POP2–waves and a control run of CESM1.2.2 (B–CTL) CO_2 flux simulations are compared with the National Oceanic and Atmospheric Administration's (NOAA) CarbonTracker, version 2022 (CT2022) data. Overall, bubbles contribute up to 41.3% to the total sea–air CO_2 flux, consistent with recent studies, and POP2–waves exhibits a stronger CO_2 flux than B–CTL under high U_{10}. Likewise, the spatial distribution of POP2–waves CO_2 flux is broadly agrees with that of NOAA CT2022, although some discrepancies remain. Under the sea–air partial pressure differences ($dp$$CO_2$) negative feedback associated with the interaction between CO_2 fluxes and the carbonate–pH system, POP2–waves show increases of 11.8%, 41.6%, and 1.8% in the CO_2 sink, source, and global average, respectively, compared to the B–CTL. The $dp$$CO_2$ (pH) exhibits the strongest positive (negative) regression coefficient with CO_2 flux across the global ocean. Additionally, K_w shows a positive (negative) regression coefficient with CO_2 flux in source (sink) regions, while SST displays the opposite pattern relative to K_w.

1. Introduction

The exchange of CO_2 between the air and sea is a crucial component of the global carbon cycle, carrying significant implications for Earth's climate (Bange et al., 2024; Friedlingstein et al., 2022; McKinley et al., 2020; Müller et al., 2023; Shutler et al., 2019). Traditionally, the exchange of CO_2 across the sea–air interface can be characterized using the following bulk formula (e.g., Wanninkhof, 1992, 2014; McKinley et al., 2020; Dong et al., 2022; Fay et al., 2021; Zhou et al., 2023; Heimdal et al., 2024):

$$FCO_2 = K_w \cdot k_0 \cdot (pCO_2^w - pCO_2^a) \cdot (1 - ice) \quad (1)$$

where the sea–air CO_2 flux (FCO_2) is determined by the gas transfer velocity (K_w), the difference in partial pressure of CO_2 (pCO_2) between the seawater and atmosphere (indicated by superscripts " w " and " a," respectively), and the solubility constant (k_0), which varies with salinity and temperature (Weiss, 1974). Moreover, the fluxes are weighted by 1 minus the ice fraction (*ice*). The estimation of bulk CO_2 fluxes in K_w is typically similar to the Wanninkhof (1992) equation:

$$K_w = 0.251 <U_{10}^2> (Sc/660)^{-0.5} \quad (2)$$

where $<U_{10}^2>$ represents the mean squared wind speed at 10 meters, and *Sc* denotes the Schmidt number. The flux estimate error can reach as high as 34% due to model limitations and uncertainties surrounding bulk parameters. (Signorini and McClain, 2009). However, significant uncertainties persist in estimates of sea–air CO_2 flux, primarily stemming from an incomplete understanding of the spatiotemporal variability in the governing mechanisms (Shutler et al., 2019).

Some studies have highlighted that estimating CO_2 fluxes involves considerations beyond just wind speed and solubility factors. Monahan and Spillane (1984) previously regarded whitecaps as "low impedance vents", effectively "shortening" the water-side transfer resistance. Without wave breaking, transport between the ocean and the atmosphere occurs through slow conduction and molecular diffusion, while breaking acts as a transitional process from laminar to turbulent flow (Deike, 2022). Bubbles offer an extra surface for gas transfer, rising through the water-side mass boundary layer of the water surface and bursting at the water surface, enhancing near-surface turbulence (Soloviev and Lukas, 2010; Bell et al., 2017; Deike and Melville, 2018; Krall et al., 2019; Czerski et al., 2022). Gutiérrez-Loza et al. (2022) pointed out that sea spray transported into the atmosphere and ultimately evaporating serves an efficient mechanism for sea–air CO_2 exchange during high and intermediate wind speeds (above 6–8 m s^{-1}), whereas during low wind speeds (<6 m s^{-1}), water-side convection was identified as a significant control mechanism. Several studies corroborate the significance of breaking waves and bubble injection mechanisms in facilitating CO_2 transfer (e.g., Andreas et al., 2016; Brumer et al., 2017; Blomquist et al., 2017; Reichl and Deike, 2020; Li et al., 2023; Zhou et al., 2023). Deike and Melville (2018) demonstrated that bubble contribution to CO_2 transfer accounts for more than 40% when the 10-meter wind speed (U_{10}) is ≥ 10 m s^{-1}, becomes dominant at $U_{10} \geq 15$ m s^{-1}, and reaches 60% at 20 m s^{-1}.

Monitoring the sea surface CO_2 content is crucial for comprehending the Earth system, as climate change has begun to impact the ocean's carbon uptake capacity (Behncke et al., 2024). However, indirect estimates of pCO_2 derived from pH and salinity measurements still entail uncertainties (e.g., Williams et al., 2017; Gray et al., 2018; Coggins et al., 2023; Behncke et al., 2024; Fay et al., 2024; Yang et al., 2024). Direct observation is the most desirable tool for understanding the real world, but the scarcity of pCO_2 and sea–air CO_2 flux measurements results in relatively short time series. The direct measurements involved discrete samples with an equilibrator system and the use of closed-path CO_2 gas analyzers to measure pCO_2 (Sutton et al., 2014, 2021; Bakker et al., 2016; Sabine et al., 2020; Akhand et al., 2021; Wu and Qi, 2023).

In addition to closed-path CO_2 measurements, direct measurements of the open-path CO_2 flux using the eddy covariance technique were conducted over the open ocean, revealing CO_2 fluxes were within a factor of 40 of those estimated by Eq. (1) (Edson et al., 2011; Tokoro et al., 2014; Bell et al., 2017; Dong et al., 2021; Van Dam et al., 2021). Local CO_2 flux observations present challenges for validating global Earth system models (ESMs) due to discrepancies in time and space scales, implementing a data assimilation system is crucial for effective model evaluation.

Several recent studies have estimated the sea–air CO_2 flux using Eq. (1), while current parameterizations in oceanic and atmospheric models still rely exclusively on wind speed (Long et al., 2013; Moore et al., 2013; Couldrey et al., 2016; Jin et al., 2017; Lovenduski et al., 2019; Ziehn et al., 2020; Chikamoto and DiNezio, 2021) and through data analysis of non-model simulations (Wanninkhof et al., 1992, 2014; Fay et al., 2021; Zhou et al., 2023). The uptake of anthropogenic CO_2 by the oceans is lowering pH and altering carbonate chemistry in nonlinear ways, further reducing the oceans' capacity to absorb additional CO_2 (Moore et al., 2013). The mechanisms of breaking waves and bubble injection in facilitating K_w have been examined primarily through data analysis of non-model simulations (e.g., Andreas et al., 2016; Blomquist et al., 2017; Reichl and Deike, 2020; Zhou et al., 2023). However, there is relatively limited discussion on the impact of wave effect mechanisms in estimating the sea–air CO_2 flux and seawater acidification within coupling the ocean biogeochemistry with wave models, whereas local processes are more tightly controlled by the sea state.

In this study, we aim to investigate the significance of breaking waves and bubble injection mechanisms through ocean geochemistry response on the sea–air CO_2 flux and ocean's buffering capacity through the carbonate–pH system, using the Parallel Ocean Program version 2 (POP2; Smith et al., 2010) of the Community Earth System Model version 1.2.2 (CESM1.2.2; Hurrell et al., 2013) coupled with waves module

https://doi.org/10.5194/egusphere-2025-4773
Preprint. Discussion started: 19 December 2025

(Mellor et al., 2008) of the Princeton Ocean Model (POM; Blumberg and Mellor, 1987). The coupled model is referred to as POP2–waves.

The structure of this paper is organized as follows. Section 2 introduces the model, data, methodology, and experiments employed in this study. The performance of the POP2–waves coupled model in simulating sea–air CO_2 flux and interaction between CO_2 flux and carbonate–pH system in Section 3, while Section 4 focuses on the impact of different configurations of waves and bubble effect on ocean geochemistry response and uncertainty arising from the absence of interactions between ocean CO_2 flux and the carbonate–pH system. Finally, Section 5 presents the conclusions.

2. Data, model experiments, and methodology

2.1 Observational data

The spatial patterns of sea–air CO_2 flux simulated by the coupled CESM1 and POP2–waves coupled model are compared with estimates from the National Oceanic and Atmospheric Administration's (NOAA) CarbonTracker modeling and data assimilation system version 2022 (CT2022; Jacobson et al., 2023), which provides global surface-atmosphere CO_2 flux estimates spanning January 2000 through December 2020. We analyzed the seasonal variations and mean states of CO_2 flux globally, especially in primary sources and sinks of CO_2 flux. Some uncertainties in the assimilation dataset arise from factors such as anthropogenic influences and ice melt; therefore, following Fay et al. (2024), this study excludes the coastal ocean and high-latitude sea regions from the model comparison.

2.2 Description of the model framework and experiments

In this study, we investigated the role of waves and bubble mechanisms through ocean geochemistry response between control POP2 and POP2–waves coupled model in CESM1.2.2 framework. The CESM simulation is conducted using a fully coupled component set over a 30-year period, with well-mixed greenhouse gases (CO_2, CH_4, N_2O, etc.), ozone, and aerosols fixed to year-2000 values (B_2000_CAM5 compsets). It has a horizontal resolution of 1.9° × 2.5° in Community Atmosphere Model 5.3 (CAM5.3) and a nominal 1° horizontal resolution with 60 vertical layers in POP2. A control CO_2 flux and seawater acidification simulation (B–CTL) uses Eq. (1), where K_w is the Wanninkhof (1992) equation (Eq. 2). We use the present-day scenario (starting from the year 2000) to estimate sea–air CO_2 flux, $pCO_2^w - pCO_2^a$ and pH across both B–CTL and POP2–waves experiments, allowing us to focus on the impact of wave effects on carbonate chemistry and to compare the results with the existing observations. In the wave effect mechanism simulations, we coupled the waves module (Mellor et al., 2008) of the POM model into POP2 (POP2–waves experiment) and incorporated bubble-mediated gas transfer, computed from a mechanistic model for air bubble entrainment at the breaking wave scale (Deike and Melville, 2018), combined with the POP2 geochemistry response.

POP2–waves experiment adopts the parameterization proposed by Deike and Melville (2018), Reichl and Deike (2020), and Deike (2022) for the bubble-mediated gas transfer velocity as a function of friction velocity, u_* (m s^{-1}) and significant wave height, H_s (m). This parameterization captures the main wave effect, as well as solubility and diffusivity, effectively consolidating for CO_2 by expressing the gas transfer velocity as the sum of the non-bubble (k_{wNB}) and bubble (k_{wB}) components, following Deike and Melville (2018):

$$K_w = K_{wNB} + K_{wB} = A_{NB} u_* \left(\frac{Sc}{660}\right)^{-1/2} + \frac{A_B}{K_0\, R\, T_0} u_*^{5/3} \, (g\, H_s)^{2/3} \qquad (3)$$

where A_{NB} is an empirical, nondimensional coefficient given as 1.55 $\times 10^{-4}$, A_B is a dimensional fitting coefficient (1.2 $\times 10^{-5}$ s^2 m^{-2}), R is the ideal gas constant (0.082 L atm mol^{-1} K^{-1}), T_0 is the sea surface temperature, SST (K), and g is gravitational acceleration (9.806 m s^{-1}). In addition, Section 3.3 will examine the contribution ratios of the non-bubble and bubble components in simulating the sea–air CO_2 flux.

2.3 Coupling POP2–waves Methodology

The architecture for the POP2–waves experiment in the CESM1.2.2 framework is shown in Fig. 1. In addition to the original component relationships in CESM1.2.2, we obtain zonal and meridional surface winds, as well as friction velocity over the ice fraction from the coupler (CPL) to calculate the wave's property and K_w. To obtain significant wave height from the wave's module, we (1) interpolate the depth-variable currents of the POP2 z-coordinates (60 levels of zonal and meridional horizontal velocity) into the POM (waves) sigma-coordinates (21 levels) for calculating the depth-dependent wave radiation equation and the specified spectrum, and (2) horizontal progression from one grid to the adjacent grid.to prevent discontinuities in wave energy at block boundaries.

3. Results

3.1 The climatological mean and seasonal variations of ocean CO_2 flux

We use the traditional sea–air CO_2 flux bulk formula (Eq. 1) in CESM1.2.2 while also incorporating the effects of waves and bubble-mediated processes with K_w, which is parameterized based on friction velocity, SST, and H_s (Eq. 3). Figure 2a–c compares the climatological mean ocean CO_2 flux (mol m^{-2} yr^{-1}; shaded) and the monthly standard deviation (SD; contours) among B–CTL, POP2–waves, and NOAA CT2022. Overall, the spatial distribution of the model-simulated CO_2 flux is broadly consistent with that of CT2022, though some discrepancies persist. The primary sources and sinks of average CO_2 flux in the Pacific simulated by the POP2–waves experiment more closely resemble those in NOAA CT2022 than those in B–CTL, although the POP2–waves experiment exhibits a larger monthly SD than B–CTL over both the Pacific and Indian Oceans. Figure 2c highlights the primary sources and sinks of CO_2 flux in the Pacific using red dashed lines, while black dashed lines denote other significant regions. Based on these highlighted areas, Fig. 2d presents 12 prominent source and sink regions identified from NOAA CT2022, selected from the 30 regions defined in the NOAA atmospheric CO_2 inversion model. These regions include: (1) Pacific Ocean – Northwestern Pacific (NWP), Eastern Equatorial Pacific (EEP), Northeastern Pacific (NEP), South Pacific Ocean 1 (SPO1), and South Pacific Ocean 2 (SPO2); (2) Indian Ocean – North Indian Ocean (NIO), South Indian Ocean 1 (SIO1), and South Indian Ocean 2 (SIO2); and (3) Atlantic Ocean – North Atlantic Ocean 1 (NAO1), North Atlantic Ocean 2 (NAO2), Equatorial Atlantic Ocean (EAO), and South Atlantic Ocean (SAO).

Figure 3 presents the nine characteristic regions of model-simulated CO_2 flux. The seasonal variations in these regions are generally consistent with those in CT2022 over the NWP, EEP, NEP, SPO1, NIO, SIO1, NAO1, EAO, and SAO. The black dashed line represents B–CTL, the red solid line represents POP2–waves, and the blue solid line represents NOAA CT2022. The bar graph shows the monthly standard deviation as a percentage of the overall range (95% minus 5%). Black hollow bars correspond to B–CTL, red bars to POP2–waves, and light blue hollow bars to NOAA CT2022. Fay et al. (2024) attributed seasonal variations in sea–air fluxes to a combination of factors, including fluctuations in SST, biological uptake of carbon dioxide, and variations in mixing and wind speeds. The percentage of monthly SD is generally within 30%, with higher values observed during the boreal winter, corresponding to strong oceanic CO_2 sinks in high-latitude regions of the Northern Hemisphere, such as NWP, NEP, and NAO1. In contrast, the Southern Hemisphere exhibits large monthly standard

https://doi.org/10.5194/egusphere-2025-4773
Preprint. Discussion started: 19 December 2025

deviations alongside relatively strong CO_2 sinks during the boreal summer in regions such as SPO1, SIO1, and SAO. Both B–CTL and POP2–waves simulations in the EEP display minimal seasonal variability in CO_2 flux, maintaining a persistent year-round efflux, consistent with the findings of Fay et al. (2024) in the equatorial Pacific. In contrast, NOAA CT2022 shows a greater degree of seasonal variability in the EEP.

Three regions—SPO2, SIO2, and NAO2—exhibit model discrepancies when compared with NOAA CT2022 (Fig. 4), which are not attributable to wave effects or the CO_2 flux bulk formula. In NAO2, both B–CTL and POP2–waves show seasonal variations similar to those in NAO1, with strong oceanic CO_2 sinks during the boreal winter, whereas NOAA CT2022 displays the opposite seasonal pattern in this region. A similar pattern is observed in SPO2, where the seasonal variations in both B–CTL and POP2–waves resemble those in SPO1 but contrast with the trend shown by NOAA CT2022.

3.2 The relationship between U_{10} and K_w over the areas of the Pacific's primary sources and sinks of CO_2 flux

The monthly gas transfer velocities for both the POP2–waves and B–CTL experiments over the smaller area of the Pacific's primary sources and sinks of CO_2 flux (Fig. 2c) is shown in Fig. 5 for (a) WP (160–180˚E, 35–40˚N, Fig. 5a) and (b) EP (230–250˚E, 0–5˚S, Fig. 5b). Gray open circles represent K_w calculated using the Wanninkhof (1992) 10-m wind speed equation (B–CTL) with their simple linear regression (SLR) and squared correlation coefficient (R^2) shown in black line and text. Green open squares represent POP2–waves data for H_s < 1.5m with the orange solid line and text indicating its SLR and R^2, while blue dots denote cases where H_s > 1.5 m with the red solid line and text depicting their SLR and R^2. Generally, the B–CTL data shows higher R^2 but lower K_w values compared to POP2–waves across all WP and EP.

https://doi.org/10.5194/egusphere-2025-4773
Preprint. Discussion started: 19 December 2025

POP2–waves exhibits a slightly lower R^2 than B–CTL due to greater deviations between K_w and U_{10}, particularly at higher surface wind speeds, consistent with the findings of Gutiérrez-Loza et al. (2022) under conditions where $H_s > 1.5$ m. Zhou et al. (2023) indicated that the wind-only formula for gas transfer velocity tends to underestimate values when U_{10} exceeds 10 m s^{-1}, and that enhanced gas transfer velocity frequently occurs under conditions of strong wave breaking and high significant wave height. These deviations occur when $U_{10} > 12$ m s^{-1} over the WP (Fig. 5a) and around $U_{10} = 9$ m s^{-1} (Fig. 5b) over the EP.

Figs. 5c and 5d display the monthly mean values of K_w for WP and EP, respectively. Red, orange solid, and black dotted lines/texts indicate POP2–waves ($H_s > 1.5$ m), average of all POP2–waves data, and B–CTL, respectively. The bar graph illustrates the monthly SD as a percentage of the overall ranking range (95% minus 5%). The annual mean value of POP2–waves K_w in WP is greater than that in EP. Figure 5c shows that WP cases with $H_s > 1.5$ m have monthly data available except in August and October, and their K_w values are higher than those from POP2–waves and B–CTL. In contrast, EP shows $H_s > 1.5$ m data only during the summer months (July to October), and the corresponding K_w values are also higher than those from POP2–waves and B–CTL. The percentage of monthly SD in the bar graph indicates no significant differences between $H_s > 1.5$ m data and POP2–waves experiments in the WP, while the K_w difference between the two datasets from January to May remains small because the average H_s during this period exceeds 1.5 m. However, in EP, a significant difference is observed between the $H_s > 1.5$ m condition and the average in POP2–waves from July to September.

3.3 Regression of CO_2 flux against U_{10} under high-wind conditions

The wind-only parameterization of gas transfer velocity tends to underestimate values when $U_{10} > 10$ m s^{-1} or $H_s > 1.5$ m (e.g., Gutiérrez-Loza et al., 2022; Zhou et al., 2023). Accordingly, Fig. 5 presents scatter plots of CO_2 flux from B–CTL and POP2–waves experiment against U_{10} (for $U_{10} > 10$ m s^{-1}) over the WP region (160–180°E, 35–40°N) to compare fluxes estimated with wind-only K_w and wave-modified K_w. High-wind conditions over the WP occur primarily in winter (42% valid data), and the associated low ocean surface temperatures further enhance CO_2 solubility. The slopes of the regression equations (–0.77 in B–CTL and –1.40 in POP2–waves) and the mean CO_2 fluxes (Y_{avg}: –6.35 in B–CTL and –6.97 in POP2–waves) both indicate that POP2–waves represents a stronger CO_2 sink in the WP region under higher wind speeds. The correlation coefficient (R) of POP2–waves is higher than that of B–CTL, indicating that the sea state–dependent K_w provides a more suitable estimate of CO_2 flux than the wind-only K_w under high-wind conditions, consistent with the findings of Gutiérrez-Loza et al. (2022) and Zhou et al. (2023).

3.4 Surface climate fields and K_w component differences between POP2–waves and B–CTL

Figures 7a–b present the surface circulation along with sea level pressure (PSL), U_{10}, and H_s, all of which are factors influencing K_w in the model. The region with $H_s > 1.5$ m is generally situated where $U_{10} > 8$ m s^{-1} and lies south of the high PSL region. Johansson et al. (2022) reported that strong winds can either fill or empty small sub-basins while simultaneously generating high waves. Similarly, the ratio of K_{wB}/K_w in POP2–waves greater than 0.5 (yellow shaded areas in Fig. 7b) mostly occurs in regions where $H_s > 1.5$ m. However, high H_s does not always correspond to a higher K_{wB}/K_w in POP2–waves, for example, in the North Pacific. Deike and Melville (2018) demonstrated that the bubble contribution to CO_2 transfer exceeds 40% when the U_{10} is ≥ 10 m s^{-1}. The bubble contribution to the total gas transfer velocity (K_{wB}/K_w) in POP2–waves is approximately 38%, which is slightly higher than ~30% reported by Reichl and Deike (2020). This discrepancy may be attributed to differences in the A_B coefficients used in this study compared to previous work. The coefficient in the sea-state formulation (A_B in Eq. (3)) is derived from field data, where gas transfer velocity is estimated from flux measurements using eddy covariance methods (Reichl and Deike, 2020; Brumer et al., 2017).

B–CTL K_w and POP2–waves K_{wNB} exhibit similar spatial distributions, with values exceeding 0.006 cm s^{-1} and 0.004 cm s^{-1}, respectively, despite using different input parameters (U_{10} vs. $u*$). Aside from the polar regions, K_w in the POP2–waves coupled model is greater than that in B–CTL with the largest differences occurring in the tropics (Fig. 7c). However, the values of K_{wNB} are approximately 30–50% lower than K_w in B–CTL (Fig. 7d).

4. Discussion

4.1 Mean State and model differences in pCO_2^w and surface pH

Previous studies have not clearly identified the discrepancy in CO_2 flux estimates between bulk formulas (e.g., Wanninkhof, 1992, 2014) and approaches that incorporate breaking waves and bubble injection to parameterize K_w in an Earth System Model. Some studies incorporate wave effects following Deike and Melville (2018), using the the Surface Ocean CO_2 Atlas (SOCAT) database (Bakker et al., 2016) to estimate CO_2 fluxes. In these approaches, CO_2 flux is treated independently of pCO_2^w values and ocean pH, with no feedback between them. Our study highlights that the ocean CO_2 system is influenced by the wave-induced K_w, affecting parameters such as alkalinity, pH, and carbonate species, which in turn feedback into the dynamics of CO_2 flux. In other words, perturbations in K_w influence both $dp\mathrm{CO_2}$ and CO_2 flux in the Earth System Model, differing from approaches that treat wave-induced K_w and $dp\mathrm{CO_2}$ independently when estimating CO_2 flux (e.g., Reichl and Deike, 2020).

Figure 8 illustrates the means and differences in the spatial distribution of pCO_2^w and pH when using the U_{10} bulk formula for K_w versus the wave-induced K_w. In B–CTL, high pCO_2^w is concentrated in the equatorial eastern Pacific (EEP), contributing to a larger oceanic CO_2 source (Fig. 2a). In contrast, low pCO_2^w is found in the high-latitude regions of the Pacific and Atlantic (e.g., NWP, NEP, NAO1, and NAO2), resulting in a strong oceanic CO_2 sink (Fig. 2a). The standard deviation of B–CTL pCO_2^w varies between 10 and 30 ppm over time (Fig. 8a).

Figure 2 shows that the CO_2 flux in POP2–waves is stronger than that in B–CTL across both source and sink regions, consistent with the higher K_w indicated by contours in Fig. 7c. Notably, POP2–waves reduces the high pCO_2^w by more than 10 ppm over the equatorial western Pacific and increases the low pCO_2^w in other regions (Fig. 8b). In the CESM1 framework, atmospheric pCO_2^a is held constant. Consequently, in source (sink) regions, the POP2-waves coupled model decreases (increases) pCO_2^w, thereby reducing $dp\mathrm{CO_2}$. This mitigates the large increase in CO_2 flux simulated by the POP2-waves model—a process referred to as 'negative feedback from $dp\mathrm{CO_2}$—and is discussed further in Section 4.3. The SD of the pCO_2^w difference between POP2–waves and B–CTL varies significantly in EEP, while SD changes in other regions are less pronounced.

Carbonic acid is a weak acid that can dissociate into bicarbonate (HCO_3^-) and hydrogen ions (H^+), thereby affecting the pH of the solution. The average pH of the ocean is currently around 8.1 (Fig. 8c), which is slightly alkaline; however, as the ocean continues to absorb more CO_2, its pH decreases, making it more acidic. Ocean pH and pCO_2^w are strongly negatively correlated (Macovei et al. 2021), with low pH values observed in the equatorial eastern Pacific (Fig. 8c), resulting from high pCO_2^w concentrations in that region (Fig. 8a). Slightly higher pH values are observed in regions with lower pCO_2^w, such as the NWP, NEP, NAO1, and NAO2. Accounting for wave effects results in simulated pH differences of approximately + (-) 0.01 in ocean source (sink) regions. This suggests that including this mechanism mitigates acidification in the equatorial Pacific but enhances ocean acidification in the NWP, NEP, NAO1, and NAO2 regions (Fig. 8d).

4.2 Impact of sea–air *dp*CO_2, K_w, SST, and pH on CO_2 flux

To determine which factor is directly associated with oceanic CO_2 flux, Fig. 9 presents the linear regression coefficients (LRC) between CO_2 flux and various normalized variables: *dp*CO_2 (Fig. 9a), K_w (Fig. 9b), SST (Fig. 9c), and pH (Fig. 9d). Here, we do not delve into the complex chemical and biochemical mechanisms in carbonate species; although, the influence of carbonate species composition, including alkalinity (ALK), and dissolved inorganic carbon (DIC), on *p*CO_2 is greater than that of solubility changes driven by sea surface salinity and SST (Koseki et al., 2023).

Among these factors, *dp*CO_2 and CO_2 flux exhibit the strongest positive LRC (0.6–0.8) across the global ocean, with the ocean acting as a CO_2 source or sink depending on whether the sea–air *dp*CO_2 is positive or negative. Additionally, wave effects increase the LRC by approximately 0.1 to 0.2, particularly in regions with strong oceanic CO_2 sources and sinks. There is a clear positive (negative) LRC between K_w and CO_2 flux in oceanic CO_2 source (sink) regions. Furthermore, wave effects reduce the absolute LRC between K_w and CO_2 flux in both oceanic CO_2 source and sink regions (Fig. 9b), indicating that wave-influenced CO_2 flux is less correlated with K_w and more closely linked to *dp*CO_2, after considering interactions between modeled CO_2 flux and the ocean carbonate-pH system.

In contrast to the former, there is a clear positive (negative) LRC between SST and CO_2 flux in oceanic CO_2 sink (source) regions (Fig. 9c). This pattern arises because CO_2 solubility increases at lower temperatures (e.g., high-latitude regions), enhancing oceanic uptake of atmospheric CO_2, whereas higher oceanic temperatures (e.g., tropical regions) reduce solubility, leading to decreased absorption and greater CO_2 release from the ocean to the atmosphere. Wave effects only slightly reduce the LRC between SST and CO_2 flux—by approximately 0.1—in the tropics, with negligible differences observed in other regions. The strong negative correlation between ocean pH and pCO_2^w is attributed to the acid dissociation constants of H_2CO_3 (Fig. 8a and 8c), which govern the relationship between dissolved CO_2 and hydrogen ion concentration (Williams et al., 2017). pH and CO_2 flux exhibit strong negative LRC (< –0.9) across the global ocean, with only a few exceptions in the EEP and along the Arctic margins (Fig. 9d). Wave effects again only slightly reduce the LRC between pH and CO_2 flux in the EEP—by approximately 0.1.

4.3 Uncertainty arising from the absence of interactions between CO_2 flux and the ocean carbonate–pH system

To assess the uncertainty in CO_2 flux resulting from the absence of interactions between CO_2 flux and the ocean carbonate–pH system (i.e., the lack of $dpCO_2$-driven negative feedback), Fig. 10a presents the CO_2 flux calculated using $dpCO_2$ values (from B–CTL) and K_w incorporating wave effects (from POP2–waves), with shading representing the mean (labeled as "no $dpCO_2$ feedback") and contours indicating their SD. Only data significant at a 95% confidence level of CO_2 flux difference between "no $dpCO_2$ feedback" and POP2–waves are shown in Fig. 10b. Compared to Fig. 2b, the CO_2 flux in the "no $dpCO_2$ feedback" case is stronger than that in the POP2–waves simulation across both source and sink regions, and is accompanied by a larger SD. The most pronounced differences occur in the Pacific source and sink regions; however, some areas (e.g., NEP, SIO2, and SPO2) do not reach the 95% confidence threshold.

The ocean's buffering capacity — including the interactions between CO_2 flux (estimated from K_w) and the ocean carbonate–pH system — incorporating wave effects mitigates pH acidification and reduces $dpCO_2$ differences over CO_2 source regions, while higher pH levels enhance the ocean's ability to absorb more CO_2 from the atmosphere over CO_2 sink regions in the POP2–waves coupled model (Fig. 8b and 8d). In contrast, the "lack of $dpCO_2$-driven negative feedback" case, which lacks real ocean buffering effects, allows CO_2 source regions to release excess CO_2 into the atmosphere and leads to increased excess CO_2 uptake in sink regions (Fig. 10b) compared to the POP2–waves coupled model.

5 Conclusions

This study quantified oceanic sea–air CO_2 fluxes using both a control run of the CESM1 model and a newly developed POP2–waves coupled model, which builds on the CESM1 framework by incorporating the effects of wave dynamics, sea surface temperature, pH, and gas transfer velocity, including interactions between CO_2 flux and the ocean carbonate–pH system. The architecture of the POP2–waves coupled model primarily addresses two challenges: (1) interpolating currents from the POP2 z-coordinate system to the sigma-coordinate system for wave radiation equation calculations, and (2) horizontal progression between adjacent grids is implemented to prevent discontinuities in wave energy at block boundaries (Fig. 1). Several recent studies have estimated the sea–air CO_2 flux using Eq. (1), although current K_w parameterizations in global models (Table 1) still rely exclusively on U_{10} (e.g., Chikamoto and DiNezio, 2021; Danabasoglu et al., 2020; Seland et al., 2020; Mauritsen et al., 2019; Ziehn et al., 2020; Lovato et al., 2022; Sigmond et al., 2023).

https://doi.org/10.5194/egusphere-2025-4773
Preprint. Discussion started: 19 December 2025

In the POP2–waves coupled model, K_w follows the parameterization proposed by Deike and Melville (2018), which relates the bubble-mediated K_w to friction velocity and significant wave height. This parameterization captures the primary wave effects, as well as solubility and diffusivity, and expresses K_w as the sum of non-bubble and bubble components in Eq. (3), which is used to compare oceanic CO_2 fluxes with estimates from NOAA CarbonTracker CT2022 data. Overall, the spatial distribution of the model-simulated CO_2 flux is broadly consistent with that of CT2022, although some discrepancies remain. The prominent source and sink regions of the average CO_2 flux simulated by the POP2–waves experiment more closely resemble those in NOAA CT2022 than those in B–CTL (Figs. 2 and 3), although notable discrepancies remain in three regions—SPO2, SIO2, and NAO2—when compared with NOAA CT2022 (Fig. 4).

We find that larger deviations between POP2–waves K_w and U_{10} occur when $H_s > 1.5$ m (Fig. 5a–b), consistent with Gutiérrez-Loza et al. (2022), indicating that POP2–waves coupled model exhibits a stronger CO_2 flux than B–CTL under high U_{10} (Fig. 6). In addition, the bubble contribution to the total gas transfer velocity (K_{wB}/K_w) in POP2–waves is approximately 38% over the entire space–time domain (Fig. 7(b)), slightly higher than the ~30% reported by Reichl and Deike (2020). These high K_{wB}/K_w regions coincide with areas of elevated H_s and U_{10}. Likewise, our results show that bubbles account for up to 41.3% of the total sea–air CO_2 flux, consistent with Zhou et al. (2023) and Reichl and Deike (2020), who reported contributions of about 40%.

POP2–waves reduce high pCO_2 by more than 10 ppm over the equatorial western Pacific and increase low pCO_2 in other regions (Fig. 8b). Wave effects also result in simulated pH differences of approximately positive (negative) 0.01 in ocean source (sink) regions (Fig. 8d). To identify the factor most directly associated with oceanic CO_2 flux, Figs. 9a and 9d shows that $dpCO_2$ (pH) exhibits the strongest positive (negative) regression coefficient across the global ocean. Additionally, K_w shows a positive (negative) regression coefficient with CO_2 flux in source (sink) regions, whereas SST displays the opposite pattern relative to K_w (Figs. 9b and 9c).

Under the *dp*CO_2-driven negative feedback associated with the interaction between CO_2 fluxes and the carbonate–pH system, POP2–waves show increases of 11.8%, 41.6%, and 1.8% in the CO_2 sink, source, and global average, respectively, compared to B–CTL. However, in the absence of *dp*CO_2-driven negative feedback, both CO_2 sink and source regions exhibit unreasonably stronger fluxes than those in POP2–waves (Fig. 10b), indicating that the increase in K_w due to wave effects—when coupled with *dp*CO_2-driven feedback—helps moderate the abnormal CO_2 flux enhancement, bringing the estimates closer to NOAA CT2022 (Fig. 3).

Finally, the effects of the K_w bulk formula (Wanninkhof et al., 1992) and wave dynamics (Deike and Melville, 2018) on sea–air CO_2 flux (arrows), surface pH (tube colors indicator), and *dp*CO_2 (circle markers) in the strongest sink (WP) and source (EP) regions during the DJF and JJA seasons are schematically summarized in Fig. 11. B–CTL is illustrated in gray with black text, while differences between POP2–waves and B–CTL are highlighted in red. Each panel features the ocean-atmosphere interface, with ocean color shading representing relative SST levels across seasons, and the SST value displayed in the lower-left corner of each panel. The B–CTL sea–air CO_2 flux shows a strong sink in DJF but only a weak sink in JJA over the WP, indicating that reduced solubility at higher SSTs weakens the oceanic CO_2 sink. POP2–waves further diminish this sink effect. The seasonal differences in *dp*CO_2, which correspond to changes in CO_2 flux and are indicated by circle markers in Fig. 11a and 11c, reveal the interaction between CO_2 flux and the ocean carbonate–pH system. In contrast, the EP region exhibits lower pH than the WP and acts as a strong CO_2 source in both DJF and JJA

(Fig. 11b and 11d), with no obvious seasonal variation (consistent with Fay et al., 2024). POP2–waves enhance the CO_2 flux but reduce the $dpCO_2$ difference.

Code and data availability. The model code of POP2–waves coupled model is available at https://doi.org/10.5281/zenodo.15795234. Input data of POP2–waves using the climatological Hadley Centre Sea Ice and Sea Surface Temperature dataset and GODAS data forcing, including 30-year numerical experiments, are available at https://doi.org/10.5281/zenodo.5510795.

Author contributions. YYL is the sole developer of the POP2–waves coupled model and writes the majority part of the paper. HHH provides computational support and analysis suggestions. WLL supports reorganization and offers analytical recommendations and SC offers a non-parallel wave module as part of the POM source code.

Competing interests. The authors declare that they have no conflict of interest.

Acknowledgements. Our deepest gratitude goes to the editors and anonymous reviewers for their careful work and thoughtful suggestions that have helped improve this paper substantially. We sincerely thank the National Center for Atmospheric Research (NCAR) and their Atmosphere Model Working Group (AMWG) for release CESM1.2.2. We are also grateful to the National Center for High- performance Computing, Taiwan for providing the facilities for the computational procedures for running POP2-waves simulations. Thanks, ChatGPT for correcting the English grammar.

Financial support. This research received funding from the Taiwan National Science and Technology Council under Grants NSTC 112-2111-M-001-008 and MOST 111-2123-M-001-007, as well as support from the Academia Sinica Grand Challenge Program in Taiwan under Grant AS-GCP-112-M03.

Reference

Akhand, A., Chanda, A., Watanabe, K., Das, S., Tokoro, T., Hazra, S., and Kuwae, T.: Reduction in riverine freshwater supply changes inorganic and organic carbon dynamics and air-water CO_2 fluxes in a tropical mangrove dominated estuary, J. Geophys. Res. G: Biogeosciences, 126, e2020JG006144, https://doi.org/10.1029/2020JG006144, 2021.

Andreas, E., Vlahos, P., and Monahan, E.: The potential role of sea spray droplets in facilitating air-sea gas transfer, in: IOP conference series: earth and environmental science, Vol. 35, p. 012003, IOP Publishing, https://doi.org/10.1088/1755-1315/35/1/012003, 2016.

Bakker, D. C. E., Pfeil, B., Landa, C. S., Metzl, N., O'Brien, K. M., Olsen, A., Smith, K., Cosca, C., Harasawa, S., Jones, S. D., Nakaoka, S., Nojiri, Y., Schuster, U., Steinhoff, T., Sweeney, C., Takahashi, T., Tilbrook, B., Wada, C., Wanninkhof, R., Alin, S. R., Balestrini, C. F., Barbero, L., Bates, N. R., Bianchi, A. A., Bonou, F., Boutin, J., Bozec, Y., Burger, E. F., Cai, W.-J., Castle, R. D., Chen, L., Chierici, M., Currie, K., Evans, W., Featherstone, C., Feely, R. A., Fransson, A., Goyet, C., Greenwood, N., Gregor, L., Hankin, S., Hardman-Mountford, N. J., Harlay, J., Hauck, J., Hoppema, M., Humphreys, M. P., Hunt, C. W., Huss, B., Ibánhez, J. S. P., Johannessen, T., Keeling, R., Kitidis, V., Körtzinger, A., Kozyr, A., Krasakopoulou, E., Kuwata, A., Landschützer, P., Lauvset, S. K., Lefèvre, N., Lo Monaco, C., Manke, A., Mathis, J. T., Merlivat, L., Millero, F. J., Monteiro, P. M. S., Munro, D. R., Murata, A., Newberger, T., Omar, A. M., Ono, T., Paterson, K., Pearce, D., Pierrot, D., Robbins, L. L., Saito, S., Salisbury, J., Schlitzer, R., Schneider, B., Schweitzer, R., Sieger, R., Skjelvan, I., Sullivan, K. F., Sutherland, S. C., Sutton, A. J., Tadokoro, K., Telszewski, M., Tuma, M., van Heuven, S. M. A. C., Vandemark, D., Ward, B., Watson, A. J., and Xu, S.: A multi-decade record of high-quality fCO_2 data in version 3 of the Surface Ocean CO_2 Atlas (SOCAT), Earth Syst. Sci. Data, 8, 383–413, https://doi.org/10.5194/essd-8-383-2016, 2016.

Bange, H. W., Mongwe, P., Shutler, J. D., Arévalo-Martínez, D. L., Bianchi, D., Lauvset, S. K., Liu, C., Löscher, C. R., Martins, H., Rosentreter, J. A., Schmale, O., Steinhoff, T., Upstill-Goddard, R. C., Wanninkhof, R., Wilson, S. T., and Xie, H.: Advances in understanding of air–sea exchange and cycling of greenhouse gases in the upper ocean, Elem Sci Anth, 12 (1), https://doi.org/10.1525/elementa.2023.00044, 2024.

Behncke, J., Landschützer, P., and Tanhua, T.: A detectable change in the air–sea CO_2 flux estimate from sailboat measurements, Sci. Rep., 14, 3345, https://doi.org/10.1038/s41598-024-53159-0, 2024.

Bell, T. G., Landwehr, S., Miller, S. D., de Bruyn, W. J., Callaghan, A. H., Scanlon, B., Ward, B., Yang, M., and Saltzman, E. S.: Estimation of bubble-mediated air–sea gas exchange from concurrent DMS and CO_2 transfer velocities at intermediate–high wind speeds, Atmos. Chem. Phys., 17, 9019–9033, https://doi.org/10.5194/acp-17-9019-2017, 2017.

Blomquist, B. W,, Brumer, S. E., Fairall, C. W., Huebert, B. J., Zappa, C. J., Brooks, I. M., Yang, M., Bariteau, L., Prytherch, J., Hare, J. E., Czerski, H., Matei, A., and Pascal, R. W.: Wind speed and sea state dependencies of air–sea gas transfer: Results from the High Wind speed Gas exchange Study (HiWinGS), J. Geophys. Res.-Ocean., 122, 8034–8062, https://doi.org/10.1002/2017JC013181, 2017.

Blumberg, A. F., and Mellor, G. L.: A Description of a Three-Dimensional Coastal Ocean Circulation Model, Costal and Estuarine Science, vol. 4, American Geophysical Union, https://doi.org/10.1029/CO004p0001, 1987.

Boucher, O., Servonnat, J., Albright, A. L., Aumont, O., Balkanski, Y., Bastrikov, V., Bekki, S., Bonnet, R., Bony, S., Bopp, L., Braconnot, P., Brockmann, P., Cadule, P., Caubel, A., Cheruy, F., Codron, F., Cozic, A., Cugnet, D., D'Andrea, F., Davini, P., de Lavergne, C., Denvil, S., Deshayes, J., Devilliers, M., Ducharne, A., Dufresne, J.-L., Dupont, E., Éthé, C., Fairhead, L., Falletti, L., Flavoni, S., Foujols, M.-A., Gardoll, S., Gastineau, G., Ghattas, J., Grandpeix, J.-Y., Guenet, B., Guez, Lionel, E., Guilyardi, E., Guimberteau, M., Hauglustaine, D., Hourdin, F., Idelkadi, A., Joussaume, S., Kageyama, M., Khodri, M., Krinner, G., Lebas, N., Levavasseur, G., Lévy, C., Li, L., Lott, F., Lurton, T., Luyssaert, S., Madec, G., Madeleine, J.-B., Maignan, F., Marchand, M., Marti, O., Mellul, L., Meurdesoif, Y., Mignot, J., Musat, I., Ottlé, C., Peylin, P., Planton, Y., Polcher, J., Rio, C., Rochetin, N., Rousset, C., Sepulchre, P., Sima, A., Swingedouw, D., Thiéblemont, R., Traore, A. K., Vancoppenolle, M., Vial, J., Vialard, J., Viovy, N., and Vuichard, N.: Presentation and Evaluation of the IPSL-CM6A-LR Climate Model, J. Adv. Model. Earth Sy., 12, e2019MS002010, https://doi.org/10.1029/2019MS002010, 2020.

Brumer, S. E., Zappa, C. J., Blomquist, B. W., Fairall, C. W., Cifuentes-Lorenzen, A., Edson, J. B., Brooks, I. M., and Huebert, B. J.: Wave-related Reynolds number parameterizations of CO_2 and DMS transfer velocities, Geophys. Res. Lett., 44, 9865–9875, https://doi.org/10.1002/2017GL074979, 2017.

Chikamoto, M. O., and DiNezio, P.: Multi-century changes in the ocean carbon cycle controlled by the tropical oceans and the Southern Ocean, Global Biogeochem. Cy., 35, e2021GB007090, https://doi.org/10.1029/2021GB007090, 2021.

Chikamoto, M. O., DiNezio, P., and Lovenduski, N.: Long-term slowdown of ocean carbon uptake by alkalinity dynamics, Geophys. Res. Lett., 50, e2022GL101954, https://doi.org/10.1029/2022GL101954, 2023.

Coggins, A., Watson, A. J., Schuster, U., Mackay, N., King, B., McDonagh, E., and Poulton, A. J.: Surface ocean carbon budget in the 2017 South Georgia diatom bloom: Observations and validation of profiling biogeochemical argo floats, Deep-Sea Res. II: Top. Stud. Oceanogr., 209, 105275. https://doi.org/10.1016/j.dsr2.2023.105275, 2023.

Couldrey, M. P., Oliver, K. I. C., Yool, A., Halloran, P. R., and Achterberg, E. P.: On which timescales do gastransfer velocities control NorthAtlantic CO_2 flux variability?, Global Biogeochem. Cy., 30,787–802, https://doi.org/10.1002/2015GB005267, 2016.

Czerski, H., Brooks, I. M., Gunn, S., Pascal, R., Matei, A., and Blomquist, B.: Ocean bubbles under high wind conditions – Part 2: Bubble size distributions and implications for models of bubble dynamics, Ocean Sci., 18, 587–608, https://doi.org/10.5194/os-18-587-2022, 2022.

Danabasoglu, G., Lamarque, J.-F., Bacmeister, J., Bailey, D. A., DuVivier, A. K., Edwards, J., Emmons, L. K., Fasullo, J., Garcia, R., Gettelman, A., Hannay, C., Holland, M. M., Large, W. G., Lauritzen, P. H., Lawrence, D. M., Lenaerts, J. T. M., Lindsay, K., Lipscomb, W. H., Mills, M. J., Neale, R., Oleson, K. W., Otto-Bliesner, B., Phillips, A. S., Sacks, W., Tilmes, S., van Kampenhout, L., Vertenstein, M., Bertini, A., Dennis, J., Deser, C., Fischer, C., Fox-Kemper, B., Kay, J. E., Kinnison, D., Kushner, P. J., Larson, V. E., Long, M. C., Mickelson, S., Moore, J. K., Nienhouse, E., Polvani, L., Rasch, P. J., and Strand, W. G.: The Community Earth System Model Version 2 (CESM2), J. Adv. Model. Earth Sy., 12, e2019MS001916, https://doi.org/10.1029/2019MS001916, 2020.

Deike, L., and Melville, W. K.: Gas transfer by breaking waves, Geophys. Res. Lett., 45, 10,482–10,492. https://doi.org/10.1029/2018GL078758, 2018.

Deike, L.: Mass transfer at the ocean-atmosphere interface: The role of wave breaking, droplets, and bubbles, Annu. Rev. Fluid Mech, 54, 191–224, https://doi.org/10.1146/annurev-fluid-030121-014132, 2022.

Dong, Y., Yang, M., Bakker, D. C. E., Kitidis, V., and Bell, T. G.:

Uncertainties in eddy covariance air–sea CO_2 flux measurements and implications for gas transfer velocity parameterisations, Atmos. Chem. Phys., 21, 8089–8110, https://doi.org/10.5194/acp-21-8089-2021, 2021.

Dong, Y., Bakker, D. C. E., Bell, T. G., Huang, B., Landschützer, P., Liss, P. S., and Yang, M.: Update on the temperature corrections of global air-sea CO_2 flux estimates, Global Biogeochem. Cy., 36, e2022GB007360, https://doi.org/10.1029/2022GB007360, 2022.

Edson, J. B., Fairall, C. W., Bariteau, L., Zappa, C. J., Cifuentes-Lorenzen, A., McGillis, W. R., Pezoa, S., Hare, J. E., and Helmig, D.: Direct covariance measurement of CO_2 gas transfer velocity during the 2008 Southern Ocean Gas Exchange Experiment: Wind speed dependency, J. Geophys. Res., 116, https://doi.org/10.1029/2011jc007022, 2011.

Fay, A. R., Gregor, L., Landschützer, P., McKinley, G. A., Gruber, N., Gehlen, M., Iida, Y., Laruelle, G. G., Rödenbeck, C., Roobaert, A., and Zeng, J.: SeaFlux: harmonization of air–sea CO_2 fluxes from surface pCO_2 data products using a standardized approach, Earth Syst. Sci. Data, 13, 4693–4710, https://doi.org/10.5194/essd-13-4693-2021, 2021.

Fay, A. R., Munro, D. R., McKinley, G. A., Pierrot, D., Sutherland, S. C., Sweeney, C., and Wanninkhof, R.: Updated climatological mean ΔfCO_2 and net sea–air CO_2 flux over the global open ocean regions, Earth Syst. Sci. Data, 16, 2123–2139, https://doi.org/10.5194/essd-16-2123-2024, 2024.

Friedlingstein, P., Jones, M. W., O'Sullivan, M., Andrew, R. M., Bakker, D. C. E., Hauck, J., Le Quéré, C., Peters, G. P., Peters, W., Pongratz, J., Sitch, S., Canadell, J. G., Ciais, P., Jackson, R. B., Alin, S. R., Anthoni, P., Bates, N. R., Becker, M., Bellouin, N., Bopp, L., Chau, T. T. T., Chevallier, F., Chini, L. P., Cronin, M., Currie, K. I., Decharme, B., Djeutchouang, L. M., Dou, X., Evans, W., Feely, R. A., Feng, L., Gasser, T., Gilfillan, D., Gkritzalis, T., Grassi, G., Gregor, L., Gruber, N., Gürses, Ö., Harris, I., Houghton, R. A., Hurtt, G. C., Iida, Y., Ilyina, T., Luijkx, I. T., Jain, A., Jones, S. D., Kato, E., Kennedy, D., Klein Goldewijk, K., Knauer, J., Korsbakken, J. I., Körtzinger, A., Landschützer, P., Lauvset, S. K., Lefèvre, N., Lienert, S., Liu, J., Marland, G., McGuire, P. C., Melton, J. R., Munro, D. R., Nabel, J. E. M. S., Nakaoka, S.-I., Niwa, Y., Ono, T., Pierrot, D., Poulter, B., Rehder, G., Resplandy, L., Robertson, E., Rödenbeck, C., Rosan, T. M., Schwinger, J., Schwingshackl, C., Séférian, R., Sutton, A. J., Sweeney, C., Tanhua, T., Tans, P. P., Tian, H., Tilbrook, B., Tubiello, F., van der Werf, G. R., Vuichard, N., Wada, C., Wanninkhof, R., Watson, A. J., Willis, D., Wiltshire, A. J., Yuan, W., Yue, C., Yue, X., Zaehle, S., and Zeng, J.: Global Carbon Budget 2021, Earth Syst. Sci. Data, 14, 1917–2005, https://doi.org/10.5194/essd-14-1917-2022, 2022.

https://doi.org/10.5194/egusphere-2025-4773
Preprint. Discussion started: 19 December 2025

Gray, A. R., Johnson, K. S., Bushinsky, S. M., Riser, S. C., Russell, J. L., Talley, L. D., Wanninkhof, R., Williams, N. L., and Sarmiento, J. L.: Autonomous biogeochemical floats detect significant carbon dioxide outgassing in the high-latitude Southern Ocean, Geophys. Res. Lett., 45(17), 9049–9057, https://doi.org/10.1029/2018GL078013, 2018.

Gutiérrez-Loza, L., Nilsson, E., Wallin, M. B., Sahlée, E., and Rutgersson, A.: On physical mechanisms enhancing air–sea CO_2 exchange, Biogeosciences, 19, 5645–5665, https://doi.org/10.5194/bg-19-5645-2022, 2022.

Hajima, T., Watanabe, M., Yamamoto, A., Tatebe, H., Noguchi, M. A., Abe, M., Ohgaito, R., Ito, A., Yamazaki, D., Okajima, H., Ito, A., Takata, K., Ogochi, K., Watanabe, S., and Kawamiya, M.: Development of the MIROC-ES2L Earth system model and the evaluation of biogeochemical processes and feedbacks, Geosci. Model Dev., 13, 2197–2244, https://doi.org/10.5194/gmd-13-2197-2020, 2020.

Heimdal, T. H., McKinley, G. A., Sutton, A. J., Fay, A. R., and Gloege, L.: Assessing improvements in global ocean $p\mathrm{CO}_2$ machine learning reconstructions with Southern Ocean autonomous sampling, Biogeosciences, 21, 2159–2176, https://doi.org/10.5194/bg-21-2159-2024, 2024.

Hurrell, J. W., Holland, M. M., Gent, P. R., Ghan, S., Kay, J. E., Kushner, P. J., Lamarque, J.-F., Large, W. G., Lawrence, D., Lindsay, K., Lipscomb, W. H., Long, M. C., Mahowald, N., Marsh, D. R., Neale, R. B., Rasch, P., Vavrus, S., Vertenstein, M., Bader, D., Collins, W. D., Hack, J. J., Kiehl, J., and Marshall, S.: The Community Earth System Model: A framework for collaborative research, Bull. Amer. Meteor. Soc., 94, 1339–1360, https://doi.org/10.1175/BAMS-D-12-00121.1, 2013.

Jacobson, A. R., Schuldt, K. N., Tans, P., Arlyn Andrews, Miller, J. B., Oda, T., Mund, J., Weir, B., Ott, L., Aalto, T., Abshire, J. B., Aikin, K., Aoki, S., Apadula, F., Arnold, S., Baier, B., Bartyzel, J., Beyersdorf, A., Biermann, T., Biraud, S. C., Boenisch, H., Brailsford, G., Brand, W. A., Chen, G., Huilin Chen, Lukasz Chmura, Clark, S., Colomb, A., Commane, R., Conil, S., Couret, C., Cox, A., Cristofanelli, P., Cuevas, E., Curcoll, R., Daube, B., Davis, K. J., Wekker, S. de, Della Coletta, J., Delmotte, M., DiGangi, E., DiGangi, J. P., Di Sarra, A. G., Dlugokencky, E., Elkins, J. W., Emmenegger, L., Shuangxi Fang, Fischer, M. L., Forster, G., Frumau, A., Galkowski, M., Gatti, L. V., Gehrlein, T., Gerbig, C., Francois Gheusi, Gloor, E., Gomez-Trueba, V., Goto, D., Griffis, T., Hammer, S., Hanson, C., Haszpra, L., Hatakka, J., Heimann, M., Heliasz, M., Hensen, A., Hermansen, O., Hintsa, E., Holst, J., Ivakhov, V., Jaffe, D. A., Jordan, A., Joubert, W., Karion, A., Kawa, S. R., Kazan, V., Keeling, R. F., Keronen, P., Kneuer, T., Kolari, P., Kateřina Komínková, Kort, E., Kozlova, E., Krummel, P., Kubistin, D., Labuschagne, C., Lam, D. H., Lan, X., Langenfelds, R. L., Laurent, O., Laurila, T., Lauvaux, T., Lavric, J., Law, B. E., Lee, J., Lee, O. S., Lehner, I., Lehtinen, K., Leppert, R., Leskinen, A., Leuenberger, M., Levin, I., Levula, J., Lin, J., Lindauer, M., Loh, Z., Lopez, M., Luijkx, I. T., Lunder, C. R., Machida, T., Mammarella, I., Manca, G., Manning, A., Manning, A., Marek, M. V., Martin, M. Y., Matsueda, H., McKain, K., Meijer, H., Meinhardt, F., Merchant, L., N. Mihalopoulos, Miles, N. L., Miller, C. E., Mitchell, L., Mölder, M., Montzka, S., Moore, F., Moossen, H., Morgan, E., Josep-Anton Morgui, Morimoto, S., Müller-Williams, J., J. William Munger, Munro, D., Myhre, C. L., Shin-Ichiro Nakaoka, Jaroslaw Necki, Newman, S., Nichol, S., Niwa, Y., Obersteiner, F., O'Doherty, S., Paplawsky, B., Peischl, J., Peltola, O., Piacentino, S., Jean-Marc Pichon, Pickers, P., Piper, S., Pitt, J., Plass-Dülmer, C., Platt, S. M., Prinzivalli, S., Ramonet, M., Ramos, R., Reyes-Sanchez, E., Richardson, S. J., Riris, H., Rivas, P. P., Ryerson, T., Saito, K., Sargent, M., Sasakawa, M., Scheeren, B., Schuck, T., Schumacher, M., Seifert, T., Sha, M. K., Shepson, P., Shook, M., Sloop, C. D., Smith, P., Stanley, K., Steinbacher, M., Stephens, B., Sweeney, C., Thoning, K., Timas, H., Torn, M., Tørseth, K., Trisolino, P., Turnbull, J., van den Bulk, P., van Dinther, D., Vermeulen, A., Viner, B., Vitkova, G., Walker, S., Watson, A., Wofsy, S. C., Worsey, J., Worthy, D., Dickon Young, Zaehle, S., Zahn, A., and Zimnoch, M.: CarbonTracker CT2022, Global Monitoring Laboratory [data set], https://doi.org/10.25925/z1gj-3254, 2023 (data available at: https://gml.noaa.gov/aftp/products/carbontracker/co2/CT2022/fluxes/monthly/, last access: 11 April 2025).

Jin, C. X., Zhou, T. J., Chen, X. L., and Wu, B: Seasonally evolving dominant interannual variability mode of air-sea CO_2 flux over the western North Pacific simulated by CESM1-BGC, Sci. China Earth Sci. 60, 1854–1865, https://doi.org/10.1007/s11430-015-9085-4, 2017.

Johansson, M. M., Björkqvist, J.-V., Särkkä, J., Leijala, U., and Kahma, K. K.: Correlation of wind waves and sea level variations on the coast of the seasonally ice-covered Gulf of Finland, Nat. Hazards Earth Syst. Sci., 22, 813–829, https://doi.org/10.5194/nhess-22-813-2022, 2022.

Koseki, S., Tjiputra, J., Fransner, F., Crespo, L. R., and Keenlyside, N. S.: isentangling the impact of Atlantic Niño on sea-air CO_2 flux. Nat. Commun. 14, 3649, https://doi.org/10.1038/s41467-023-38718-9, 2023.

Krall, K. E., Smith, A. W., Takagaki, N., and Jähne, B.: Air–sea gas exchange at wind speeds up to 85 m s^{-1}, Ocean Sci., 15, 1783–1799, https://doi.org/10.5194/os-15-1783-2019, 2019.

Li, S, Babanin, A. V., and Guan, C.: Dimensionless Parameterizations of Air-Sea CO2 Gas Transfer Velocity on Surface Waves, Tellus B: Chem. Phys. Meteorol., 75(1), 1–12, https://doi.org/10.16993/

tellusb.1867, 2023.

Liu, B., Six, K. D., and Ilyina, T.: Incorporating the stable carbon isotope 13C in the ocean biogeochemical component of the Max Planck Institute Earth System Model, Biogeosciences, 18, 4389–4429, https://doi.org/10.5194/bg-18-4389-2021, 2021.

Long, M. C., Lindsay, K., Peacock, S., Moore, J. K., and Doney, S. C.: Twentieth-Century oceanic carbon uptake and storage in CESM1(BGC), J. Climate, 26, 6775–6800, https://doi.org/10.1175/JCLI-D-12-00184.1, 2013.

Lovato, T., Peano, D., Butenschön, M., Materia, S., Iovino, D., Scoccimarro, E., Fogli, P. G., Cherchi, A., Bellucci, A., Gualdi, S., Masina, S., and Navarra, A.: CMIP6 Simulations With the CMCC Earth System Model (CMCC-ESM2), J. Adv. Model. Earth Sy., 14, e2021MS002814, https://doi.org/10.1029/2021MS002814, 2022.

Lovenduski, N. S., Yeager, S. G., Lindsay, K., and Long, M. C.: Predicting near-term variability in ocean carbon uptake, Earth Syst. Dynam., 10, 45–57, https://doi.org/10.5194/esd-10-45-2019, 2019.

Macovei, V. A., Petersen, W., Brix, H., and Voynova, Y. G.: Reduced ocean carbon sink in the south and central North Sea (2014–2018) revealed from FerryBox observations Geophys. Res. Lett., 48, e2021GL092645, https://doi.org/10.1029/2021GL092645, 2021.

Mauritsen, T., Bader, J., Becker, T., Behrens, J., Bittner, M., Brokopf, R., Brovkin, V., Claussen, M., Crueger, T., Esch, M., Fast, I., Fiedler, S., Flaeschner, D., Gayler, V., Giorgetta, M., Goll, D. S., Haak, H., Hagemann, S., Hedemann, C., Hohenegger, C., Ilyina, T., Jahns, T., Jimenéz-de-la Cuesta, D., Jungclaus, J., Kleinen, T., Kloster, S., Kracher, D., Kinne, S., Kleberg, D., Lasslop, G., Kornblueh, L., Marotzke, J., Matei, D., Meraner, K., Mikolajewicz, U., Modali, K., Moebis, B., Mueller, W. A., Nabel, J. E. M. S., Nam, C. C. W., Notz, D., Nyawira, S.-S., Paulsen, H., Peters, K., Pincus, R., Pohlmann, H., Pongratz, J., Popp, M., Raddatz, T. J., Rast, S., Redler, R., Reick, C. H., Rohrschneider, T., Schemann, V., Schmidt, H., Schnur, R., Schulzweida, U., Six, K. D., Stein, L., Stemmler, I., Stevens, B., von Storch, J.-S., Tian, F., Voigt, A., Vrese, P., Wieners, K.-H., Wilkenskjeld, S., Winkler, A., and Roeckner, E.: Developments in the MPI-M Earth System Model version 1.2 (MPI-ESM1.2) and Its Response to Increasing CO_2, J. Adv. Model. Earth Sy., 11, 998–1038, https://doi.org/10.1029/2018MS001400, 2019.

McKinley, G. A., Fay, A. R., Eddebbar, Y. A., Gloege, L., and Lovenduski, N. S.: External forcing explains recentdecadal variability of the ocean carbonsink, AGU Advances, 1,e2019AV00014, https://doi.org/10.1029/2019AV000149, 2020.

Mellor, G. L., Donelan, M. A., and Oey, L.-Y.: A surface wave model for coupling with numerical ocean circulation models. J. Atmos. Ocean. Technol., 25(10), 1785–1807, https://doi.org/10.1175/2008JTECHO573.1, 2008.

Monahan, E. C., and Spillane, M. C.: The role of oceanic whitecaps in air-sea gas exchange, in: Gas transfer at water surfaces, edited by: Brutsaert, W. and Jirka, G. H., Reidel, Hingham, MA, 495–503, https://doi.org/10.1007/978-94-017-1660-4_45, 1984.

Moore, J. K., Lindsay, K., Doney, S. C., Long, M. C., and Misumi, K.: Marine ecosystem dynamics and biogeochemical cycling in the Community Earth System Model [CESM1 (BGC)]: Comparison of the 1990s with the 2090s under the RCP4. 5 and RCP8. 5 scenarios, J. Climate, 26, 9291–9312, https://doi.org/10.1175/JCLI-D-12-00566.1, 2013.

Müller, J. D., Gruber, N., Carter, B., Feely, R., Ishii, M., Lange, N., Lauvset, S. K., Murata, A., Olsen, A., Pérez, F. F., Sabine, C., Tanhua, T., Wanninkhof, R., and Zhu, D.: Decadal trends in the oceanic storage of anthropogenic carbon from 1994 to 2014. AGU Advances, 4, e2023AV000875, https://doi.org/10.1029/2023AV000875, 2023.

Reichl, B. G., and Deike, L.: Contribution of sea-state dependentbubbles to air-sea carbon dioxidefluxes, Geophys. Res. Lett., 47, e2020GL087267. https://doi.org/10.1029/2020GL087267, 2020.

Roobaert, A., Resplandy, L., Laruelle, G. G., Liao, E., and Regnier, P.: Unraveling the physical and biological controls of the global coastal CO_2 sink, Global Biogeochem. Cy., 38, e2023GB007799. https://doi.org/10.1029/2023GB007799, 2024.

Sabine, C., Sutton, A., McCabe, K., Lawrence-Slavas, N., Alin, S, Feely, R., Jenkins, R., Maenner, S., Meinig, C., Thomas, J., van Ooijen, E., Passmore, A., and Tilbrook, B.: Evaluation of a new carbon dioxide system for autonomous surface vehicles, J. Atmos. Oceaen. Tech., 37, 1305–1317, https://doi.org/10.1175/JTECH-D-20-0010.1, 2020.

Séférian, R., Nabat, P., Michou, M., Saint-Martin, D., Voldoire, A., Colin, J., Decharme, B., Delire, C., Berthet, S., Chevallier, M., Sénési, S., Franchisteguy, L., Vial, J., Mallet, M., Joetzjer, E., Geoffroy, O., Guérémy, J.-F., Moine, M.-P., Msadek, R., Ribes, A., Rocher, M., Roehrig, R., Salas-y-Mélia, D., Sanchez, E., Terray, L., Valcke, S., Waldman, R., Aumont, O., Bopp, L., Deshayes, J., Éthé, C., and Madec, G.: Evaluation of CNRM Earth-System model, CNRM-ESM2-1: role of Earth system processes in present-day and future climate, J. Adv. Model. Earth Sy., 11, 4182–4227, https://doi.org/10.1029/2019MS001791, 2019.

Seland, Ø., Bentsen, M., Olivié, D., Toniazzo, T., Gjermundsen, A., Graff, L. S., Debernard, J. B., Gupta, A. K., He, Y.-C., Kirkevåg, A., Schwinger, J., Tjiputra, J., Aas, K. S., Bethke, I., Fan, Y., Griesfeller, J., Grini, A., Guo, C., Ilicak, M., Karset, I. H. H., Landgren, O., Liakka, J., Moseid, K. O., Nummelin, A., Spensberger, C., Tang, H., Zhang, Z., Heinze, C., Iversen, T., and Schulz, M.:

Overview of the Norwegian Earth System Model (NorESM2) and key climate response of CMIP6 DECK, historical, and scenario simulations, Geosci. Model Dev., 13, 6165–6200, https://doi.org/10.5194/gmd-13-6165-2020, 2020.

Shutler, J. D., Wanninkhof, R., Nightingale, P. D., Woolf, D. K., Bakker, D. C., Watson, A., Ashton, I., Holding, T., Chapron, B., Quilfen, Y., Fairall, C., Schuster, U., Nakajima, M., and Donlon, C. J.: Satellites will address critical science priorities for quantifying ocean carbon, Front. Ecol. Environ., 18(1): 27–35, http://dx.doi.org/10.1002/fee.2129, 2019.

Sigmond, M., Anstey, J., Arora, V., Digby, R., Gillett, N., Kharin, V., Merryfield, W., Reader, C., Scinocca, J., Swart, N., Virgin, J., Abraham, C., Cole, J., Lambert, N., Lee, W.-S., Liang, Y., Malinina, E., Rieger, L., von Salzen, K., Seiler, C., Seinen, C., Shao, A., Sospedra-Alfonso, R., Wang, L., and Yang, D.: Improvements in the Canadian Earth System Model (CanESM) through systematic model analysis: CanESM5.0 and CanESM5.1, Geosci. Model Dev., 16, 6553–6591, https://doi.org/10.5194/gmd-16-6553-2023, 2023.

Signorini, S. R., and McClain, C. R.: Effect of uncertainties in climatologic wind, ocean $p\mathrm{CO}_2$, and gas transfer algorithms on the estimate of global sea–air CO_2 flux, Global Biogeochem. Cy., 23, GB2025, https://doi.org/10.1029/2008GB003246, 2009.

Smith, R., Jones, P., Briegleb, B., Bryan, F., Danabasoglu, G., Dennis, J., Dukowicz, J., Eden, C., Fox-Kemper, B., Gent, P., Hecht, M., Jayne, S., Jochum, M., Large, W., Lindsay, K., Maltrud, M., Norton, N., Peacock, S., Vertenstein, M., and Yeager, S.: The Parallel Ocean Program (POP) reference manual ocean component of the Community Climate System Model (CCSM) and Community Earth System Model (CESM), Los Alamos National Laboratory Tech. Rep. LAUR-10-01853, 140 pp, https://www2.cesm.ucar.edu/models/cesm1.0/pop2/doc/sci/POPRefManual.pdf, 2010.

Soloviev, A., and Lukas, R.: Effects of Bubbles and Sea Spray on Air–Sea Exchange in Hurricane Conditions, Bound.-Layer Meteorol., 136, 365–376, https://doi.org/10.1007/s10546-010-9505-0, 2010.

Stock, C. A., Dunne, J. P., Fan, S., Ginoux, P., John, J., Krasting, J. P., Laufkötter, C., Paulot, F., and Zadeh, N.: Ocean biogeochemistry in GFDL's Earth System Model 4.1 and its response to increasing atmospheric CO_2, J. Adv. Model. Earth Sy., 12, e2019MS002043, https://doi.org/10.1029/2019MS002043, 2020.

Sutton, A. J., Sabine, C. L., Maenner-Jones, S., Lawrence-Slavas, N., Meinig, C., Feely, R. A., Mathis, J. T., Musielewicz, S., Bott, R., McLain, P. D., Fought, H. J., and Kozyr, A.: A high-frequency atmospheric and seawater $p\mathrm{CO}_2$ data set from 14 open-ocean sites using a moored autonomous system, Earth Syst. Sci. Data, 6, 353–

366, https://doi.org/10.5194/essd-6-353-2014, 2014.

Tjiputra, J. F., Schwinger, J., Bentsen, M., Morée, A. L., Gao, S., Bethke, I., Heinze, C., Goris, N., Gupta, A., He, Y.-C., Olivié, D., Seland, Ø., and Schulz, M.: Ocean biogeochemistry in the Norwegian Earth System Model version 2 (NorESM2), Geosci. Model Dev., 13, 2393–2431, https://doi.org/10.5194/gmd-13-2393-2020, 2020.

Tokoro, T., Hosokawa, S., Miyoshi, E., Tada, K., Watanabe, K., Montani, S., Kayanne, H., and Kuwae, T.: Net uptake of atmospheric CO_2 by coastal submerged aquatic vegetation, Glob. Change Biol., 20, 1873–1884, https://doi.org/10.1111/gcb.12543, 2014.

Van Dam, B., Polsenaere, P., Barreras-Apodaca, A., Lopes, C., Sanchez-Mejia, Z., Tokoro, T., Kuwae, T., Loza, L. G., Rutgersson, A., Fourqurean, J., and Thomas, H.: Global trends in air-water CO_2 exchange over seagrass meadows revealed by atmospheric Eddy Covariance, Global Biogeochem. Cy., 35, e2020GB006848, https://doi.org/10.1029/2020GB006848, 2021.

Wanninkhof, R.: Relationship between wind speed and gas exchange over the ocean, J. Geophys. Res., 97(C5), 7373–7382. https://doi.org/10.1029/92JC00188, 1992.

Wanninkhof, R.: Relationship between wind speed and gas exchange over the ocean revisited, Limnol. Oceanogr.: Methods, 12(6), 351–362. https://doi.org/10.4319/lom.2014.12.351, 2014.

Weiss, R. F.: Carbon dioxide in water and seawater: the solubility of a non-ideal gas, Mar. Chem., 2 (3), pp. 203-215, https://doi.org/10.1016/0304-4203(74)90015-2, 1974.

Williams, N. L., Juranek, L. W., Feely, R. A., Johnson, K. S., Sarmiento, J. L., Talley, L. D., Dickson, A. G., Gray, A. R., Wanninkhof, R., Russell, J. L., and Riser, S. C.: Calculating surface ocean pCO_2 from biogeochemical Argo floats equipped with pH: An uncertainty analysis, Global Biogeochem. Cy., 31, 591–604, https://doi.org/10.1002/2016GB005541, 2017.

Wu, Y., and Qi, D.: The controversial Southern Ocean air-sea CO_2 flux in the era of autonomous ocean observations, Sci. Bull., 68, 21, 2519-2522, https://doi.org/10.1016/j.scib.2023.08.059, 2023.

Yang, X., Wynn-Edwards, C. A., Strutton, P. G., and Shadwick, E. H.: Drivers of air-sea CO_2 flux in the subantarctic zone revealed by time series observations. Global Biogeochem. Cy., 38, e2023GB007766, https://doi.org/10.1029/2023GB007766, 2024.

Yool, A., Palmiéri, J., Jones, C. G., de Mora, L., Kuhlbrodt, T., Popova, E. E., Nurser, A. J. G., Hirschi, J., Blaker, A. T., Coward, A. C., Blockley, E. W., and Sellar, A. A.: Evaluating the physical and biogeochemical state of the global ocean component of UKESM1 in CMIP6 historical simulations, Geosci. Model Dev., 14, 3437–3472, https://doi.org/10.5194/gmd-14-3437-2021, 2021.

Zhou, X., Reichl, B. G., Romero, L., and Deike, L.: A sea state dependent gas transfer velocity for CO_2 unifying theory, model, and field data, Earth Space Sci., 10, e2023EA003237, https://doi.org/10.1029/2023EA003237, 2023.

Ziehn, T., Chamberlain, M., Law, R., Lenton, A., Bodman, R., Dix, M., Stevens, L., Wang, Y.-P., and Srbinovsky, J.: The Australian Earth System Model: ACCESS-ESM1.5, J. South. Hemisph. Earth Syst. Sci., 70(1) 193-214, https://doi.org/10.1071/ES19035, 2020.

https://doi.org/10.5194/egusphere-2025-4773
Preprint. Discussion started: 19 December 2025

Table 1. Intercomparison of Earth System Model for estimating sea–air CO_2 flux

Earth System Model	Ocean components	CO_2 flux consider waves	K_w's element	Reference
CESM1	POP2	no	U_{10} (Wannikhof 1992)	Chikamoto and DiNezio, 2021; Chikamoto et al., 2023
CESM2	POP2	no	U_{10} (Wannikhof 2014)	Danabasoglu et al., 2020
NorESM2	BLOM	no	U_{10} (Wannikhof 2014)	Seland et al., 2020; Tjiputra et al., 2020
MPI-ESM1.2	MPIOM 1.6	no	U_{10} (Wannikhof 2014)	Mauritsen et al., 2019; Liu et al., 2021
ACCESS-ESM1.5	MOM5	no	U_{10} (Wannikhof 1992)	Ziehn et al., 2020
CMCC-ESM2	NEMO v3.6	no	U_{10} (Wannikhof 1992)	Lovato et al., 2022
CanESM5	CanNEMO	no	U_{10} (Wannikhof 1992)	Sigmond et al., 2023
GFDL-ESM4.1	MOM6	no	U_{10} (Wannikhof 2014)	Stock et al., 2020; Roobaert et al., 2024
IPSL-CM6A-LR	NEMO-PISCES	no	U_{10} (Wannikhof 1992)	Boucher et al., 2020
MIROC-ES2L	COCO 4.0	no	U_{10} (Wannikhof 1992)	Hajima et al., 2020
UKESM1	NEMO v3.6	no	U_{10} (Wannikhof 1992)	Yool et al., 2021
CNRM-ESM2-1	NEMO-PISCES	no	U_{10} (Wannikhof 1992)	Séférian et al., 2019
CESM1-POP2–waves	POP2–wave coupled model	Yes	H_s, u* (Deike and Melville, 2018)	This study

Note: CESM1: the Community Earth System Model version 1 of the National Center for Atmospheric Research (NCAR); CESM2: CESM version 2; POP2: the Parallel Ocean Program version 2; NorESM2: The Norwegian Earth System Model version 2; BLOM: Bergen Layered Ocean Model; MPI-ESM1.2: the Max Planck Institute for Meteorology Earth System Model version 1.2; MPIOM 1.6: the Max-Planck Institute Ocean Model version 1.6; ACCESS-ESM1.5: the Australian Community Climate and Earth System Simulator form an Earth System Model version 1.5; MOM5: the GFDL Modular Ocean Model version 5; CMCC-ESM2: the Euro-Mediterranean Centre on Climate Change (CMCC) Earth System Model version 2; NEMO v3.6: Nucleus for European Modelling of the Ocean version 3.6; CanESM5: the Canadian Earth System Model version 5; CanNEMO: NEMO version 3.4 modified for CanESM; GFDL-ESM4.1: the Geophysical Fluid Dynamics Laboratory's Earth System Model 4.1; MOM6: the GFDL Modular Ocean Model version 6; IPSL-CM6A-LR :version 6 of the Institut Pierre-Simon Laplace (IPSL) climate model; NEMO-PISCES: Nucleus for European Modelling of the Ocean, Pelagic Interaction Scheme for Carbon and Ecosystem Studies ocean general circulation and biogeochemistry model; MIROC-ES2L: the Model for Interdisciplinary Research on Climate, Earth System version 2; COCO 4.0: CCSR (Center for Climate System Research) Ocean Component Model version 4.0: UKESM1: the U.K. Earth System Model; CNRM-ESM2-1: the Earth system (ES) model of second generation developed by the Centre National de Recherches Météorologiques (CNRM); CESM1-POP2–wave: POP2–waves coupled model based on CESM1.

Figure List

Figure 1. Architecture diagram for POP2–waves experiment in CESM1.2.2 framework, including components for the atmosphere [Community Atmosphere Model version 5 (CAM5)], land [Community Land Model version 4 (CLM4)], ocean [Parallel Ocean Program, version 2 (POP2), waves module (waves), and the Message Passing Interface (MPI) utilities], sea ice [prognostic Los Alamos Sea Ice Model (CICE)], and the coupler (CPL).

Figure 2. Climatological mean of ocean CO_2 flux (mol m^{-2} yr^{-1}; shaded) and monthly standard deviation (SD: contour): (a) B–CTL; (b) POP2–waves; (c) NOAA CT2022: red dashed lines highlight the primary sources and sinks of CO_2 flux in the Pacific, while black dashed lines denote other significant areas; (d) Based on NOAA CT2022, 12 prominent source and sink regions have been identified among the 30 areas in the NOAA atmospheric CO_2 inversion model. These include: (1) Pacific Ocean – Northwestern Pacific (NWP), Eastern Equatorial Pacific (EEP), Northeastern Pacific (NEP), South Pacific Ocean 1 (SPO1), and South Pacific Ocean 2 (SPO2); (2) Indian Ocean – North Indian Ocean (NIO), South Indian Ocean 1 (SIO1), and South Indian Ocean 2 (SIO2); (3) Atlantic Ocean – North Atlantic Ocean 1 (NAO1), North Atlantic Ocean 2 (NAO2), Equatorial Atlantic Ocean (EAO), and South Atlantic Ocean (SAO).

Figure 3. The monthly mean values of the high-correlation climatological average of CO_2 flux with NOAA CT2022 are based on nine characteristic regions (NWP, EEP, NEP, SPO1, NIO, SIO1, NAO1, EAO, and SAO) shown in Fig. 2d. The black dashed line represents B–CTL, the red solid line represents POP2–waves, and the blue solid line represents NOAA CT2022. The bar graph illustrates the monthly standard deviation as a percentage of the overall ranking range (95% minus 5%). Black hollow bars correspond to B–CTL, red solid bars to POP2–waves, and light blue hollow bars to NOAA CT2022.

Figure 4. Same as Fig. 3, but for the low-correlation climatological average of the simulated CO_2 flux compared with NOAA CT2022, based on the three characteristic regions (SPO2, SIO2, and NAO2).

Figure 5. Scatter plots of gas transfer velocity (K_w) versus U_{10} for (a) the Western Pacific (WP; 160–180°E, 35–40°N) and (b) the Eastern Pacific (EP; 230–250°E, 0–5°S). Gray open circles, green open squares, and blue dots with black edges represent B–CTL, POP2–waves data for $H_s < 1.5$ m, and $H_s > 1.5$ m, respectively.

Corresponding simple linear regressions (SLRs) and squared correlation coefficients (R^2) are shown with black dotted lines/text (B–CTL), orange solid lines/text (POP2–waves, $H_s < 1.5$ m), and red solid lines/text (POP2–waves, $H_s > 1.5$ m). Panels (c) and (d) display the monthly mean values of K_w for WP and EP, respectively. Red and orange solid lines/text indicate POP2–waves ($H_s > 1.5$ m) and the average of all POP2–waves data, while the black dotted line/text represents B–CTL. red hollow bars for POP2–waves ($H_s > 1.5$ m), orange for average POP2–waves, and black for B–CTL.

Figure 6. Scatter plots of CO_2 flux (Kw) versus U_{10} with regression lines over the Western Pacific (160–180°E, 35–40°N) under high-wind conditions ($U_{10} > 10$ m s^{-1}) for (a) B–CTL and (b) POP2–waves experiments. Black dots indicate monthly mean values from each experiment. Blue lines denote the 95% and 5% confidence limits of the mean response, while red lines denote the 95% and 5% prediction intervals. The regression equation (Y = mx + b), correlation coefficient (R), mean CO_2 flux (Yavg), and standard deviation (YSD) are shown to the right of the legend.

Figure 7. The average gas transfer velocity is influenced by the atmospheric factor and its corresponding ratio, as depicted in the figure: (a) Shaded areas represent 10-m wind speed (U_{10}, m s^{-1}), with contours indicating sea level pressure (PSL, mb). (b) The ratio of bubble-mediated components (K_{wB}) to POP2–waves K_w is shown in color, with contours representing significant wave height (m). (c) Shaded areas represent K_w (B–CTL), with contours depicting the ratios of K_w ((POP2–waves−B–CTL)/B–CTL). (d) Shaded areas show the non-bubble-mediated component (K_{wNB}), while contours represent the ratios of (K_{wNB}− K_w (B–CTL))/K_w (B–CTL).

Figure 8. The 30-year average and model difference of pCO_2 (ppm; panels a and b) and ocean surface pH (panels c and d), with the average represented by shading and the standard deviation by contours. Panels (a) and (c) present results from the B–CTL experiment, while panels (b) and (d) depict the differences between the POP2–waves and B–CTL experiments with a T-score corresponding to a 95% confidence level.

Figure 9. The 30-year averages of the linear regression coefficients (LRC) between CO_2 flux and (a) $dpCO_2$, (b) K_w, (c) SST, and (d) pH are shown for B–CTL (shaded), with contours representing differences between POP2–waves and B–CTL. White areas indicate LRCs that are insignificant at the 95% confidence level. All variables were normalized before regression.

Figure 10. Estimated CO_2 flux assuming lack of *dp*CO_2-driven negative feedback. (a) CO_2 flux calculated using independent *dp*CO_2 values (from B–CTL) and K_w incorporating wave effects (labeled as "lack of *dp*CO_2-driven negative feedback"), with shading representing the mean and contours indicating the SD, (b) Difference in CO_2 flux between the "lack of *dp*CO_2-driven negative feedback" case and the POP2–waves simulation, with shading for the mean difference and contours for the SD passing a 95% confidence level.

Figure 11. Schematic diagrams illustrate B–CTL (gray colors) and the differences between POP2–waves and B–CTL (red colors) in CO_2 flux (arrows), surface pH (tube colors indicator), and sea–air $dpCO_2$ (circle markers) over the CO_2 sink (WP) and CO_2 source (EP). Each panel includes an ocean-atmosphere interface, with ocean color shading representing relative SST levels across different seasons. The lower-left corner displays the SST value, (a) WP in DJF seasonal mean, (b) EP in DJF seasonal mean, (c) WP in JJA seasonal mean, and (d) EP in JJA seasonal mean.

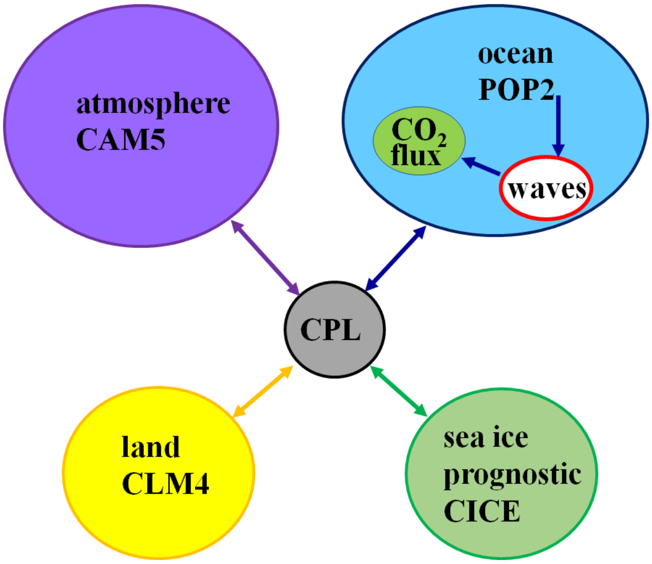

Figure 1. Architecture diagram for POP2–waves experiment in CESM1.2.2 framework, including components for the atmosphere [Community Atmosphere Model version 5 (CAM5)], land [Community Land Model version 4 (CLM4)], ocean [Parallel Ocean Program, version 2 (POP2), waves module (waves), sea ice [prognostic Los Alamos Sea Ice Model (CICE)], and the coupler (CPL).

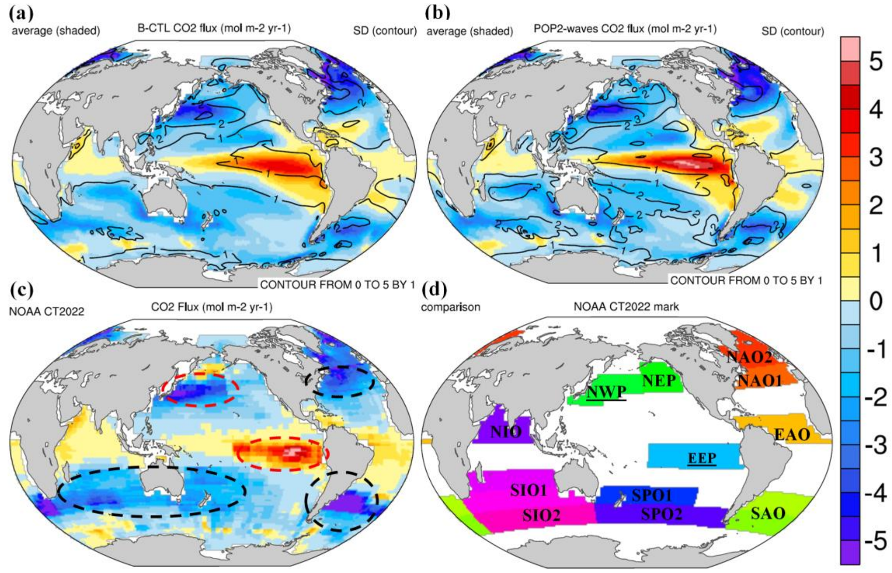

Figure 2. Climatological mean of ocean CO_2 flux (mol m^{-2} yr^{-1}; shaded) and monthly standard deviation (SD: contour): (a) B–CTL; (b) POP2–waves; (c) NOAA CT2022: red dashed lines highlight the primary sources and sinks of CO_2 flux in the Pacific, while black dashed lines denote other significant areas; (d) Based on NOAA CT2022, 12 prominent source and sink regions have been identified among the 30 areas in the NOAA atmospheric CO_2 inversion model. These include: (1) Pacific Ocean – Northwestern Pacific (NWP), Eastern Equatorial Pacific (EEP), Northeastern Pacific (NEP), South Pacific Ocean 1 (SPO1), and South Pacific Ocean 2 (SPO2); (2) Indian Ocean – North Indian Ocean (NIO), South Indian Ocean 1 (SIO1), and South Indian Ocean 2 (SIO2); (3) Atlantic Ocean – North Atlantic Ocean 1 (NAO1), North Atlantic Ocean 2 (NAO2), Equatorial Atlantic Ocean (EAO), and South Atlantic Ocean (SAO).

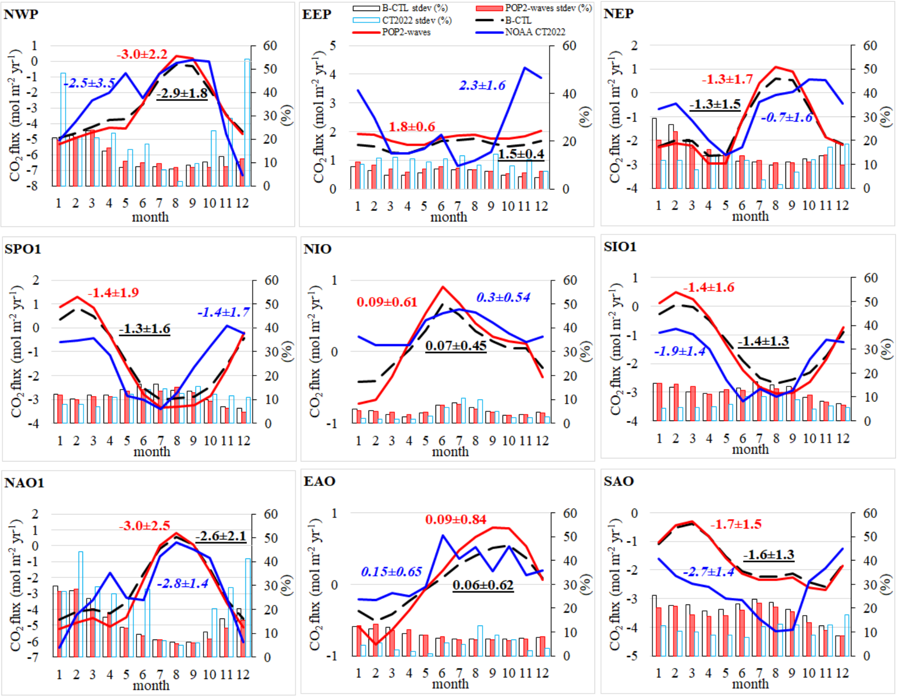

Figure 3. The monthly mean values of the high-correlation climatological average of CO₂ flux with NOAA CT2022 are based on nine characteristic regions (NWP, EEP, NEP, SPO1, NIO, SIO1, NAO1, EAO, and SAO) shown in Fig. 2d. The black dashed line represents B–CTL, the red solid line represents POP2–waves, and the blue solid line represents NOAA CT2022. The bar graph illustrates the monthly standard deviation as a percentage of the overall ranking range (95% minus 5%). Black hollow bars correspond to B–CTL, red solid bars to POP2–waves, and light blue hollow bars to NOAA CT2022.

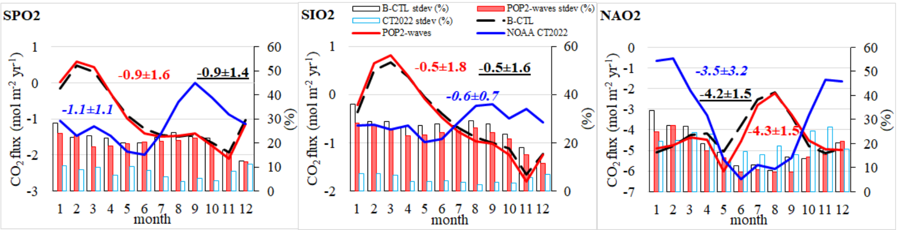

Figure 4. Same as Fig. 3, but for the low-correlation climatological average of the simulated CO_2 flux compared with NOAA CT2022, based on the three characteristic regions (SPO2, SIO2, and NAO2).

https://doi.org/10.5194/egusphere-2025-4773
Preprint. Discussion started: 19 December 2025

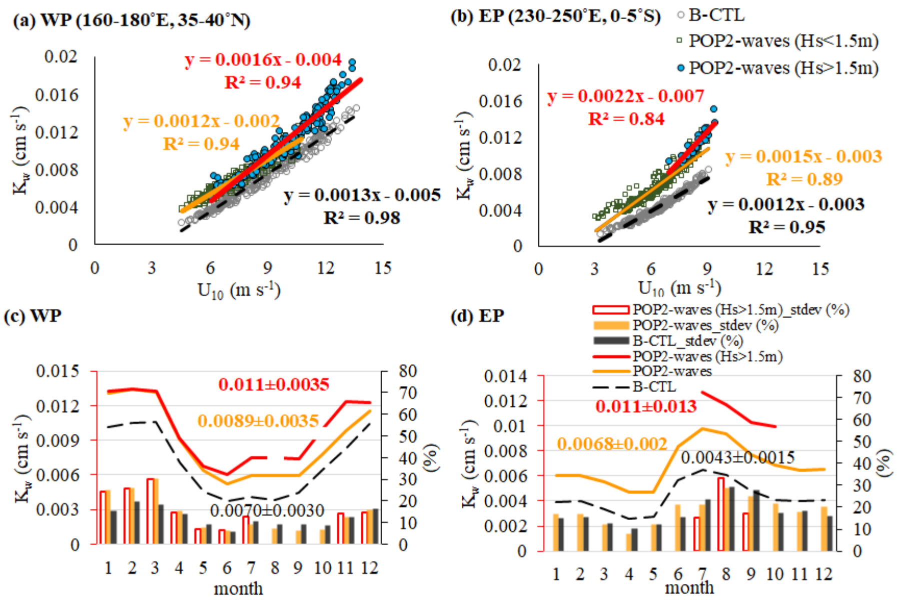

Figure 5. Scatter plots of gas transfer velocity (K_w) versus U_{10} for (a) the Western Pacific (WP; 160–180°E, 35–40°N) and (b) the Eastern Pacific (EP; 230–250°E, 0–5°S). Gray open circles, green open squares, and blue dots with black edges represent B–CTL, POP2–waves data for $H_s < 1.5$ m, and $H_s > 1.5$ m, respectively. Corresponding simple linear regressions (SLRs) and squared correlation coefficients (R^2) are shown with black dotted lines/text (B–CTL), orange solid lines/text (POP2–waves, $H_s < 1.5$ m), and red solid lines/text (POP2–waves, $H_s > 1.5$ m). Panels (c) and (d) display the monthly mean values of K_w for WP and EP, respectively. Red and orange solid lines/text indicate POP2–waves ($H_s > 1.5$ m) and the average of all POP2–waves data, while the black dotted line/text represents B–CTL. red hollow bars for POP2–waves ($H_s > 1.5$ m), orange for average POP2–waves, and black for B–CTL.

https://doi.org/10.5194/egusphere-2025-4773
Preprint. Discussion started: 19 December 2025

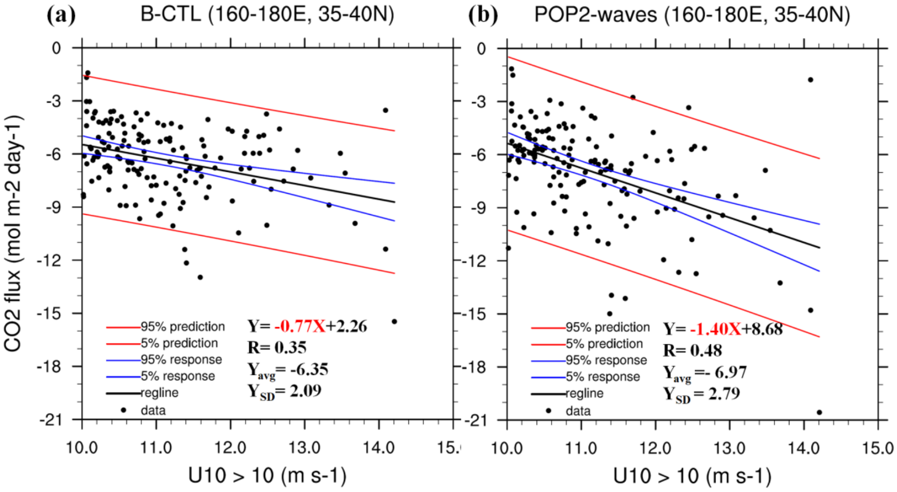

Figure 6. Scatter plots of CO_2 flux (K_w) versus U_{10} with regression lines over the Western Pacific (160–180°E, 35–40°N) under high-wind conditions ($U_{10} > 10$ m s^{-1}) for (a) B–CTL and (b) POP2–waves experiments. Black dots indicate monthly mean values from each experiment. Blue lines denote the 95% and 5% confidence limits of the mean response, while red lines denote the 95% and 5% prediction intervals. The regression equation (Y = mx + b), correlation coefficient (R), mean CO_2 flux (Y_{avg}), and standard deviation (Y_{SD}) are shown to the right of the legend.

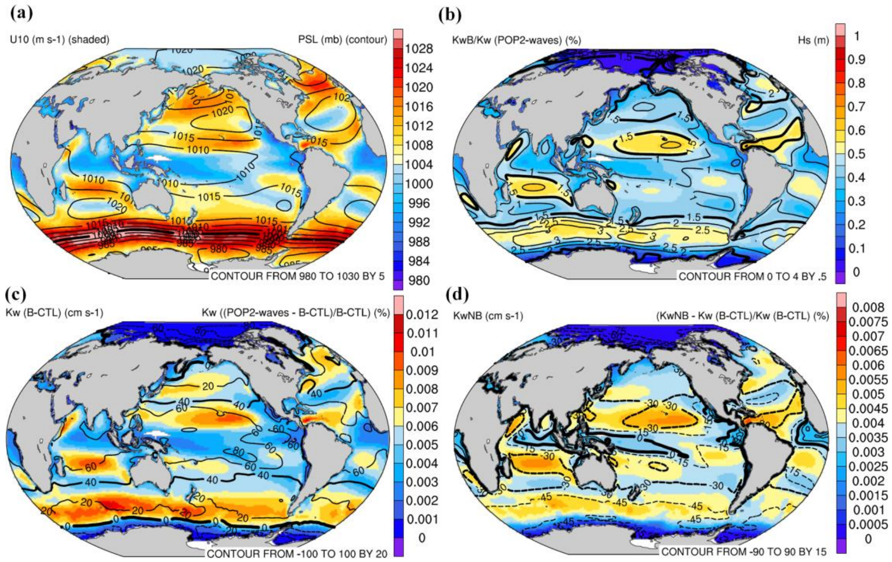

Figure 7. The average gas transfer velocity is influenced by the atmospheric factor and its corresponding ratio, as depicted in the figure: (a) Shaded areas represent 10-m wind speed (U_{10}, m s^{-1}), with contours indicating sea level pressure (PSL, mb). (b) The ratio of bubble-mediated components (K_{wB}) to POP2–waves K_w is shown in color, with contours representing significant wave height (m). (c) Shaded areas represent K_w (B–CTL), with contours depicting the ratios of K_w ((POP2–waves−B–CTL)/B–CTL). (d) Shaded areas show the non-bubble-mediated component (K_{wNB}), while contours represent the ratios of (K_{wNB}− K_w (B–CTL))/K_w (B–CTL).

https://doi.org/10.5194/egusphere-2025-4773
Preprint. Discussion started: 19 December 2025

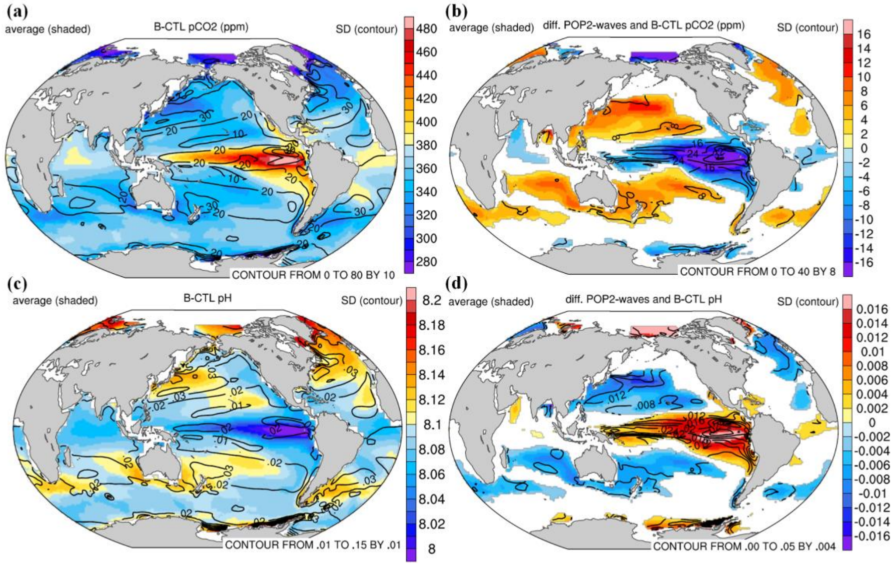

Figure 8. The 30-year average and model difference of pCO_2 (ppm; panels a and b) and ocean surface pH (panels c and d), with the average represented by shading and the standard deviation by contours. Panels (a) and (c) present results from the B–CTL experiment, while panels (b) and (d) depict the differences between the POP2–waves and B–CTL experiments with a T-score corresponding to a 95% confidence level.

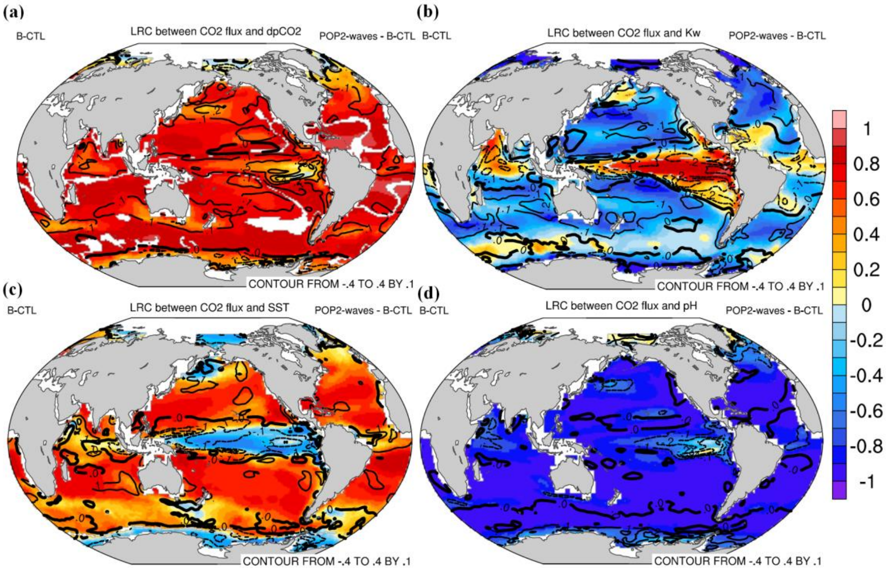

Figure 9. The 30-year averages of the linear regression coefficients (LRC) between CO_2 flux and (a) $dpCO_2$, (b) K_w, (c) SST, and (d) pH are shown for B–CTL (shaded), with contours representing differences between POP2–waves and B–CTL. White areas indicate LRCs that are insignificant at the 95% confidence level. All variables were normalized before regression.

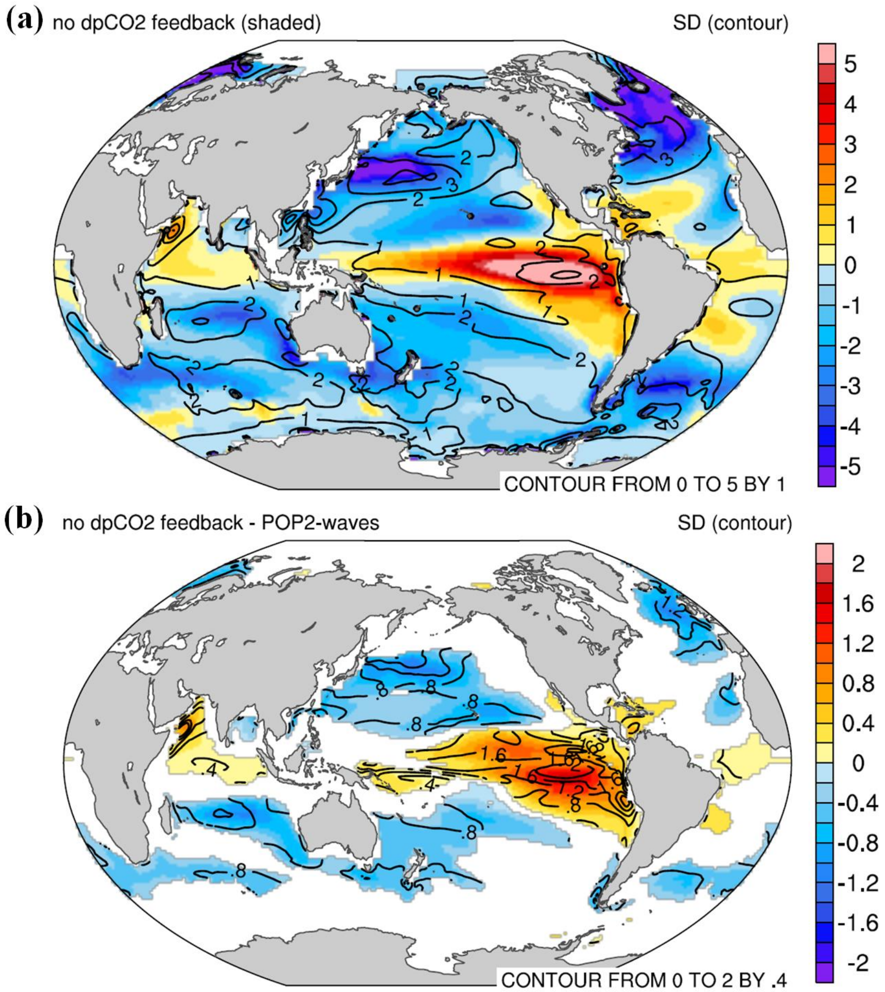

Figure 10. Estimated CO_2 flux assuming lack of *dp*CO_2-driven negative feedback. (a) CO_2 flux calculated using independent *dp*CO_2 values (from B–CTL) and K_w incorporating wave effects (labeled as "lack of *dp*CO_2-driven negative feedback"), with shading representing the mean and contours indicating the SD, (b) Difference in CO_2 flux between the "lack of *dp*CO_2-driven negative feedback" case and the POP2–waves simulation, with shading for the mean difference and contours for the SD passing a 95% confidence level.

https://doi.org/10.5194/egusphere-2025-4773
Preprint. Discussion started: 19 December 2025

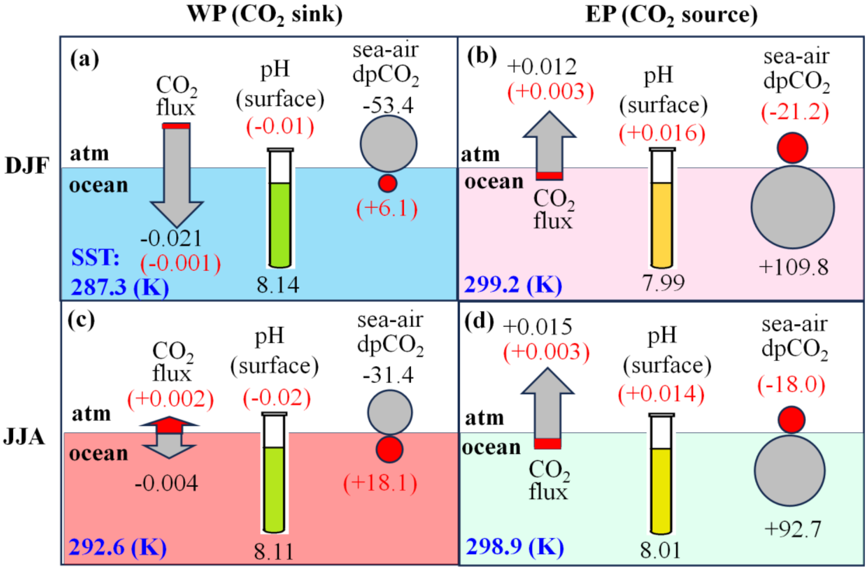

Figure 11. Schematic diagrams illustrate B–CTL (gray colors) and the differences between POP2–waves and B–CTL (red colors) in CO_2 flux (arrows), surface pH (tube colors indicator), and sea–air *dpCO₂* (circle markers) over the CO_2 sink (WP) and CO_2 source (EP). Each panel includes an ocean-atmosphere interface, with ocean color shading representing relative SST levels across different seasons. The lower-left corner displays the SST value, (a) WP in DJF seasonal mean, (b) EP in DJF seasonal mean, (c) WP in JJA seasonal mean, and (d) EP in JJA seasonal mean.